

Notice

This manuscript is peer-reviewed manuscript that has been accepted and published with open access in Journal of Geophysical Research: Solid Earth.

The manuscript can be cited as follows:

Heimisson, E. R., Rudnicki, J., & Lapusta, N. (2021). Dilatancy and compaction of a rate-and-state fault in a poroelastic medium: Linearized stability analysis. *Journal of Geophysical Research: Solid Earth*, 126, e2021JB022071. <https://doi.org/10.1029/2021JB022071>

The version submitted to EarthArXiv is the final submitted version prior to acceptance. The official published version and the EarthArXiv one will differ slightly in copy editing, typesetting, and formatting, but not in terms of scientific content and results.

Contact: elias.heimisson@sed.ethz.ch

Dilatancy and compaction of a rate-and-state fault in a poroelastic medium: Linearized stability analysis

Elías Rafn Heimisson^{1,2}, John Rudnicki³, Nadia Lapusta^{1,4}

¹Seismological Laboratory, California Institute of Technology, Pasadena, CA, USA

²Now at: Swiss Seismological Service, ETH Zurich, Zurich, Switzerland

³Department of Civil and Environmental Engineering and Department of Mechanical Engineering,

Northwestern University, Evanston, IL, USA

⁴Department of Mechanical and Civil Engineering, California Institute of Technology, Pasadena,

California, USA

Key Points:

- We analyze stability of a rate-and-state fault in a poroelastic solid with fully coupled dilatancy
- We show that dilatancy stabilization can also occur in a highly diffusive bulk if shear zone permeability is low
- We identify a new stabilizing mechanism associated with the mechanical expansion of the shear zone

Corresponding author: Elías Rafn Heimisson, eheimiss@caltech.edu,
elias.heimisson@sed.ethz.ch

Abstract

Faults in the crust at seismogenic depths are embedded in a fluid-saturated, elastic, porous material. Slip on such faults may induce transient pore pressure changes through dilatancy or compaction of the gouge or host rock. However, the poroelastic nature of the crust and the full coupling of inelastic gouge processes and the host rock have been largely neglected in previous analyses. Here, we present a linearized stability analysis of a rate-and-state fault at steady-state sliding in a fully-coupled poroelastic solid under in-plane and anti-plane sliding. We further account for dilatancy of the shear zone and the associated pore pressure changes in an averaged sense. We derive the continuum equivalent of the analysis by Segall and Rice (1995) and highlight a new parameter regime where dilatancy stabilization can act in a highly diffusive solid. Such stabilization is permitted since the time scale of flux through the shear zone and diffusion into the bulk can be very different. A novel aspect of this study involves analyzing the mechanical expansion of the shear layer causing fault-normal displacements, which we describe by a mass balance of the solid constituent of the gouge. This effect gives rise to a universal stabilization mechanism in both drained and undrained limits. The importance of the mechanism scales with shear-zone thickness and it is significant for wider shear zones exceeding approximately 1 cm. We hypothesize that this stabilization mechanism may alter and delay an ongoing shear localization process.

1 Introduction

Recently, the role of fluids in faults has received great interest for two main reasons: first, by the discovery of a strong causal link between fluid injection and induced seismicity (e.g., Ellsworth, 2013); second, by the mounting evidence that slow slip and tremor are generated at high ambient fluid pressures (e.g., Bürgmann, 2018). A topic of notable recent interest in studies of induced seismicity is the role of poroelasticity. The slow slip and tremor literature has been significantly influenced by the idea of dilatancy and how dilatancy can stabilize fault slip and generate slow slip events. Recently, it has become clear that the topics of slow slip and aseismic transients in nature and human-induced seismicity are closely linked. For example, Bhattacharya and Viesca (2019) and Viesca and Dublanche (2019) have shown how spontaneous aseismic and slow slip transients arise on faults subject to pore-pressure changes. Torberntsson et al. (2018) investigated slow and fast slip in response to fluid injection near a fault in a poroelastic solid.

49 Further, dilatancy as a stabilizing mechanism for faults subjected to fluid injection has
50 been studied recently (Ciardo & Lecampion, 2019). This study combines both poroe-
51 lasticity and dilatancy to understand frictional sliding in a fully coupled sense, where pore
52 pressure changes of the shear zone influence the bulk and vice versa. In this introduc-
53 tion, we start by discussing poroelasticity, then we review the concept of dilatancy, and
54 finally we provide an overview of the paper.

55 Biot’s theory of poroelasticity has gained much interest in the study of induced seis-
56 micity (Segall & Lu, 2015) because fluid injection does not only change pore pressure,
57 but also induces long-ranging stress interactions through the coupling of fluid pressure
58 and straining of the porous rock. It is well established that the crust behaves as a poroe-
59 lastic solid (Jónsson et al., 2003) and thus Biot’s theory of poroelasticity offers a more
60 realistic way to model the earth’s crust than simple elasticity.

61 The role of poroelasticity in the propagation of shear cracks and frictional sliding
62 has been a subject of interest for decades (Rice & Simons, 1976; Rice & Cleary, 1976;
63 Rudnicki & Koutsibelas, 1991; Rudnicki & Rice, 2006; Dunham & Rice, 2008; Heimis-
64 son et al., 2019). Perhaps the most intriguing aspect of this problem is the role of the
65 pore pressure changes during in-plane, or mode II, sliding. Such sliding induces volumet-
66 ric stress change on both sides of the fault plane, whereas anti-plane or mode III slid-
67 ing does not induce volumetric stress. During in-plane sliding, the volumetric stress change
68 is compressive on one side and expansive on the other, with a discontinuity across the
69 plane. This raises an important question of which pore pressure should be used to com-
70 pute the effective normal stress at the frictional interface. Field observations of faults
71 suggest that the principal slip zone often lies at the boundary of the damage zone and
72 the fault core (F. M. Chester et al., 1993, 2004; Dor et al., 2006). The fault core gener-
73 ally has a much lower permeability than the damage zone (Wibberley & Shimamoto, 2003).
74 In models that idealize the fault core as an impermeable surface, the relevant pore pres-
75 sure is often taken to be the value at an infinitesimal distance from the shear zone (pre-
76 sented as p^+ or p^- in Figure 1a but no core depicted) (Rudnicki & Koutsibelas, 1991;
77 Rudnicki & Rice, 2006; Dunham & Rice, 2008; Heimisson et al., 2019). Another view
78 was presented by Jha and Juanes (2014), in which shear localization occurs preferentially
79 in the fault core where effective normal stress is low and thus the relevant pore pressure
80 is where it is highest on either side of the fault core. However, such a model requires the
81 shear localization zone to be able to change sides dynamically in the core depending on

82 how the normal stress evolves. We conclude that significant uncertainty remains regard-
83 ing how slip-induced pore pressure changes interact with the shear zone and/or fault core
84 and dynamically change the effective normal stress.

85 Here, we introduce a somewhat conservative and simplified view and select the av-
86 erage pore pressure through the shear zone as the relevant pore pressure for computing
87 the effective normal stress. We allow the shear zone to have a different permeability than
88 the host rock. This choice of the relevant pore pressure implies that the shear-zone width
89 is initially at steady state and not localizing or delocalizing at any relevant frictional or
90 diffusional time scale. As we explain in more detail in the next section, the problem of
91 selecting the appropriate pore pressure for shear of a finite-width fault zone in a poroe-
92 lastic medium remains largely unsolved and likely needs explicit modeling.

93 When sheared and perturbed, e.g., due to changes in slip speed, the fault gouge
94 can dilate or compact. The process changes the void volume fraction of the gouge, which
95 is also approximately the porosity of the gouge. If the volume change occurs faster than
96 the fluid pressure can equilibrate, then the changes in the void volume fraction can dra-
97 matically alter the pore pressure. Much like other processes of frictional interfaces, the
98 influence of these volume changes on frictional strength has not been derived from first
99 principles. The related models and theory have been largely derived and developed based
100 on empirical observations (e.g. Marone et al., 1990; Lockner & Byerlee, 1994; Proctor
101 et al., 2020). Nevertheless, the process can be understood as the result of continuous re-
102 arranging and deformation of grains in the gouge to accommodate sliding. Based on ex-
103 perimental results (Marone et al., 1990), Segall and Rice (1995) postulated, following the
104 critical state concept in soil mechanics, the existence of a steady-state void volume (or
105 porosity) which establishes itself eventually for sliding at steady state with a given con-
106 stant slip velocity. If the slip speed increases or decreases, the granular structure dilates
107 or compacts, respectively. Dilatancy and compaction are well established from labora-
108 tory frictional experiments spanning three decades (e.g. Marone et al., 1990; Lockner
109 & Byerlee, 1994; Proctor et al., 2020) and have been attributed to strain-rate harden-
110 ing of visco-plastic asperity contacts in simulations of rough interfaces (Hulikal et al.,
111 2018) as well as the dynamics of grains in simulations of granular media without viscoplas-
112 ticity (Ferdowsi & Rubin, 2020). In addition to being induced by shear of granular ma-
113 terials, dilatancy is well known to accompany inelastic deformation of brittle rocks (Brace
114 et al., 1966) and can be induced by earthquake nucleation and rupture (Templeton &

115 Rice, 2008; Lyakhovsky & Ben-Zion, 2020). Dilatancy accompanying earthquake nucle-
 116 ation and rupture will likely happen at a different scale than the granular dilatancy and
 117 further increase the complexity of pore-pressure changes in the vicinity of the shear-zone
 118 (Viesca et al., 2008). In this paper we will not further consider this type of dilatancy.

Segall and Rice (1995) used the laboratory observations of Marone et al. (1990),
 which documented porosity changes in a velocity-stepping experiment under drained con-
 ditions, to propose a model for the observed porosity changes. They postulated the ex-
 istence of a steady-state porosity which depends on the slip velocity and to which the
 porosity evolves with slip:

$$\dot{\phi} = -\frac{V}{L} \left(\phi - \phi_0 - \gamma \log \left(\frac{V}{V_0} \right) \right), \quad (1)$$

119 where ϕ_0 is the steady-state porosity at the reference slip speed V_0 , L is the character-
 120 istic state evolution distance and γ is an empirical dilatancy coefficient. Segall and Rice
 121 (1995) also proposed a related dilatancy model in which the porosity depends on the fric-
 122 tional state variable that reflects the evolution of the sliding surface(here equation 33).
 123 Near steady-state sliding, the two models behave the same, but some differences occur
 124 away from the steady state. Recent experiments have suggested that a state-variable for-
 125 mulation may be more appropriate (Proctor et al., 2020). We emphasize that even though
 126 γ is referred to as a dilatancy coefficient, the formulations by Segall and Rice (1995) de-
 127 scribe both dilatancy and compaction, or alternatively void volume changes.

128 Segall and Rice (1995) then coupled the dilatancy model with a simple single-degree-
 129 of-freedom spring slider system and a membrane diffusion model (Rudnicki & Chen, 1988)
 130 and carried out a linearized stability analysis and numerical simulations. This work was
 131 revisited by Segall et al. (2010) who expanded previous work on the spring-slider sta-
 132 bility analysis and explored a more elaborate homogenous diffusion model. However, the
 133 main goal of Segall et al. (2010) was to explore dilatancy as a mechanism that can quench
 134 earthquake instability and generate slow slip. Models using dilatancy for stabilization
 135 have found agreement with observed behavior of subduction zone slow-slip events (e.g.,
 136 Segall et al., 2010; Liu, 2013; Dal Zilio et al., 2020). These models go beyond the spring-
 137 slider analysis and explore a rate-and-state fault with dilatancy coupled to an elastic con-
 138 tinuum. However, to date, dilatancy coupled to a poroelastic bulk, as we do here, has
 139 not been explored.

140 In this study, we formulate a closed system of equations and carry out a linearized
 141 stability analysis of a rate-and-state fault with dilatancy coupled to a poroelastic bulk.
 142 Further, we allow the shear zone to have different diffusivity from the bulk.

143 The paper starts by discussing the governing equations, boundary conditions, and
 144 various effects that may arise from frictional sliding and dilatancy or compaction in a
 145 poroelastic solid. That section concludes by presenting solutions for stresses and pore
 146 pressures at the fault in a joint Fourier-Laplace transform domain. The following sec-
 147 tion derives various constitutive relationship for the shear layers and presents the rate-
 148 and-state friction law. The section concludes with the mathematical formulation of the
 149 linearized stability analysis. Finally, we present the results and derive several simple ap-
 150 proximations that characterize stability in certain limiting cases. The section concludes
 151 by comparing these approximations to the full solutions to the characteristic equation
 152 obtained through a standard root-finding algorithm.

153 2 Problem statement and boundary conditions

154 We consider two poroelastic half spaces with interface at $y = 0$ that are uniformly
 155 sliding past each other with slip rate V_0 across the interface which is spatially and tem-
 156 porally uniform. V_0 is small enough such that inertial effects and wave-mediated stress
 157 transfer can be ignored. The interface is at a uniform shear stress τ_0 and effective nor-
 158 mal stress σ_0 and thus friction coefficient $f_0 = \tau_0/\sigma_0$. The pore pressure p is also at
 159 equilibrium and spatially uniform. At time $t = 0$, this steady-state configuration is per-
 160 turbed by introducing a Fourier mode slip perturbation $\delta_x = e^{st+ikx}$, with the total slip
 161 for $t > 0$ being $V_0 t + \delta_x$. This non-uniform (or heterogeneous) slip excites spatial vari-
 162 ation in slip speed, shear stress, pore-pressure, and normal stress.

163 The displacements u_i and pressure changes p relative to an equilibrium pressure
 164 state are governed four coupled partial differential equations. These are (e.g., Detour-
 165 nay & Cheng, 1995)

$$Gu_{i,kk} + \frac{G}{1-2\nu}u_{k,ki} = \alpha p_{,i} \quad (2)$$

166 and

$$\frac{1}{M}p_{,t} - \kappa p_{,kk} = -\alpha u_{k,kt}, \quad (3)$$

167 where u_i are displacements and we have assumed that body forces are negligible. The
 168 equations are presented in the index notation. Subscript ", t " indicates the partial deriva-
 169 tive with respect to time, subscript ", i " indicates the partial derivative with respect to
 170 the spatial coordinate i . Index $i = 1$ refers to the x axis, which lies in the fault plane.
 171 Index $i = 2$ refers to the y axis that is perpendicular to the fault plane. Finally, index
 172 $i = 3$ corresponds to the z axis, but all fields will be assumed invariant in that direc-
 173 tion since we will conduct a plane-strain analysis. Repeated indices such as " kk " rep-
 174 resent sum over all spatial indices. Finally, the material parameters are denoted as fol-
 175 lows, G : shear modulus, ν : drained Poisson's ratio, α : Biot-Willis parameter, M : Biot
 176 modulus. Finally, κ is the mobility, which is defined as the ratio between the permeabil-
 177 ity and fluid viscosity. Later we shall replace some of these parameters with other poroe-
 178 lastic parameters for more compact and intuitive expressions. In Appendix A, we pro-
 179 vide expressions for converting between poroelastic parameters and Table A1 with im-
 180 portant fixed parameters.

181 Under the assumption of the plane strain, the four coupled equations above can
 182 be decoupled and written out in terms of displacement functions \mathcal{E} and \mathcal{S} derived by Verruijt
 183 (1971); McNamee and Gibson (1960), but see also Detournay and Cheng (1995) for a
 184 more pedagogical description. We follow the procedure outlined in the Appendix of Heimisson
 185 et al. (2019), but solve the system of equations for a more general set of boundary con-
 186 ditions:

$$\lim_{y \rightarrow 0^\pm} u_x^+ - u_x^- = \delta_x, \quad (4)$$

$$\lim_{y \rightarrow 0^\pm} u_y^+ - u_y^- = \delta_y, \quad (5)$$

$$\lim_{y \rightarrow \pm\infty} u_i^\pm = 0, \quad (6)$$

$$\lim_{y \rightarrow \pm\infty} p^\pm = 0, \quad (7)$$

$$\lim_{y \rightarrow 0^\pm} \sigma_{xy}^+ - \sigma_{xy}^- = 0, \quad (8)$$

$$\lim_{y \rightarrow 0^\pm} \sigma_{yy}^+ - \sigma_{yy}^- = 0, \quad (9)$$

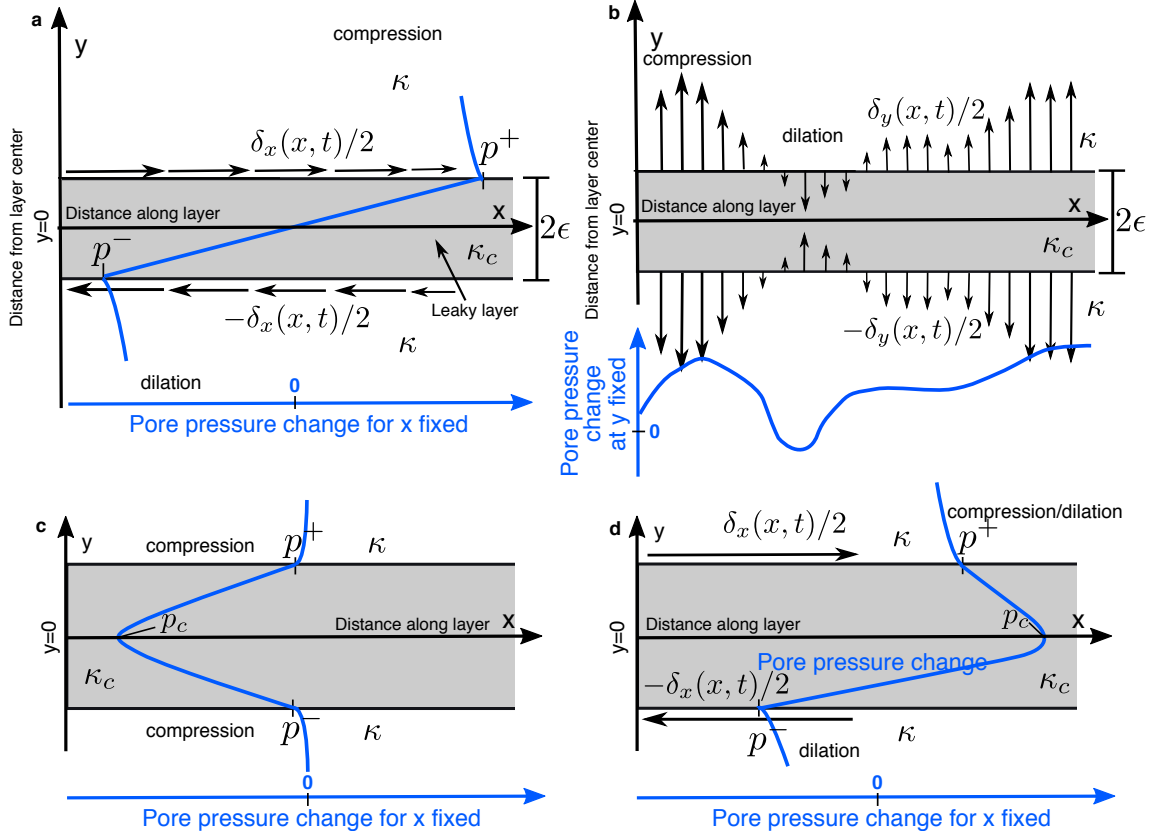


Figure 1. We explore various ways in which the deformation of a leaky and pressurized thin shearing layer of thickness 2ϵ and mobility κ_c , which we consider to be the shear zone, may couple to the surrounding poroelastic medium of mobility κ . **a** In-plane shear across the thin layer (indicated by horizontal arrows) compresses the bulk material on one side of the shear crack tip and dilates the material on the other. Due to poroelastic coupling, this increases pore pressure on the compressive side of the layer and decreases the pore pressure on the dilation side. This case, in which changes from pore pressure arise only from slip $\delta_x(x, t)$, was explored by Heimisson et al. (2019). **b** Processes in the thin layer, such as injection or inelastic dilation/compaction, may cause the layer to contract or expand (as indicated by vertical arrows), which would cause pore pressure changes in the surrounding medium. For example, expansion of the layer (outward facing arrows) would compress the the bulk (as indicated by the word "compression") and raise pore pressure in the bulk. **c** Internal pore pressure decrease can occur in the layer, $p_c(x, t) < 0$, perhaps due to inelastic dilation. The flow of pore fluids into the layer from the surrounding medium would cause compression adjacent to the layer in the bulk. **d** An example of a situation that combines changes in the pore pressure $p_c(x, t)$ in the layer (an increase in this case, e.g., due to fluid injection) and bulk effects of shear across the layer. The bulk material adjacent to the fault may undergo both compression and dilation (due to slip) and dilation due to pore pressure flow from the fault to the bulk if pressure $p_c(x, t)$ exceeds the slip induced pressure changes at the boundary, as shown.

187 where + and – superscripts refer to the $y > 0$ and $y < 0$ half-spaces respectively, and
 188 σ_{xy}^+ , σ_{xy}^- , σ_{yy}^+ , and σ_{yy}^- refer to the shear and normal perturbations in stress on top of
 189 the initial uniform values. We note that boundary conditions are applied at $y \rightarrow 0^\pm$,
 190 which contains a layer with thickness 2ϵ as shown in Figure 1. We assume that the layer
 191 is "thin" and can be treated through the boundary conditions at $y \rightarrow 0^\pm$. In other words,
 192 we require that $\epsilon \ll \lambda_{min}$, where λ_{min} is the smallest length-scale over which any phys-
 193 ical fields vary along the x axis. This can be regarded as a boundary layer approach where
 194 the outer solution treats the shear zone as a mathematical zero-thickness interface, but
 195 the inner solution treats it as having a finite thickness.

196 The first two boundary conditions describe the deformation of the thin layer by ar-
 197 bitrary shearing, contraction, or expansion of the layer. The displacement discontinu-
 198 ities δ_x and δ_y across the layer are presented as occurring at the boundaries (Figure 1a-
 199 b). However, as long as the layer is thin, these displacements could be internal to the
 200 layer. For example $\delta_x(x, t)$ could both represent an infinitesimally thin slip surface within
 201 the layer (e.g., Heimisson et al., 2019), or it could represent a distributed shear through-
 202 out the layer.

203 The third and fourth boundary conditions guarantee that the displacements and
 204 pressure changes vanish at $y \rightarrow \pm\infty$. The fifth and sixth boundary conditions enforce
 205 that shear and normal stress are continuous across the layer. This condition also makes
 206 sense only for a thin layer.

207 Finally, we formulate a boundary condition for the pore pressure at the layer bound-
 208 ary. First, we recognize that this layer may generate pore pressure changes through sev-
 209 eral processes that may be slip-dependent, such as compaction or dilation (Segall & Rice,
 210 1995), chemical such as dehydration reactions, or simply due to applied perturbations
 211 from, for example, injection into the shear layer. Second, we recognize that such inter-
 212 face layers are generally produced by frictional wear, and such alterations may dramat-
 213 ically change the permeability (e.g. Caine et al., 1996; Wibberley & Shimamoto, 2003;
 214 Behnken & Faulkner, 2011). The difference in pore pressure at the boundary relative to
 215 the internal pore pressure determines the direction of the fluid flux. Taking $p_c(x, t)$ to
 216 be the pore pressure in the center of the layer (Figure 1 c-d), we can approximate the
 217 pressure gradient on the \pm sides of the layer as $(p^\pm - p_c)/\epsilon$. We use Darcy's law to pro-

218 vide a flux boundary condition that equates the fluid flux out of each side of the layer
 219 to the flux into the bulk:

$$\left. \frac{dp^\pm}{dy} \right|_{y=0^\pm} = \pm \frac{\kappa_c}{\kappa} \frac{(p^\pm - p_c)}{\epsilon}, \quad (10)$$

220 where κ_c is the mobility within the shear layer. Equation (10) generalizes the leaky plane
 221 boundary condition of Song and Rudnicki (2017) and reduces to it if $p_c = 0$. Note that
 222 Equation (10) can result in an asymmetric flux out of the layer.

223 If we assume that equation (10) holds rigorously, then the pore pressure in the layer
 224 can be written as follows:

$$\begin{aligned} p(y) &= \frac{y}{\epsilon}(p^+ - p_c) + p_c & \text{if } 0 < y < \epsilon \\ p(y) &= \frac{y}{\epsilon}(p_c - p^-) + p_c & \text{if } -\epsilon < y < 0. \end{aligned} \quad (11)$$

225 **2.1 Solutions to slip and pore pressure changes in Fourier-Laplace do-**
 226 **main: In-plane shear**

227 Let us define the joint Fourier-Laplace transform:

$$\bar{\hat{\delta}}_x(s, k) = \int_0^\infty \int_{-\infty}^\infty \delta_x(t, x) e^{-ikx-st} dx dt, \quad (12)$$

228 applied here to the slip $\delta_x(x, t)$, or displacement discontinuity across the layer in the x
 229 direction, where the bar symbol represents the Laplace transform in time and the hat
 230 represents the Fourier transform along the x spatial axis. Some symbols may not carry
 231 the hat symbol if they are explicitly written out in terms of wavenumber k .

232 Following the procedure outlined by Heimisson et al. (2019), we derive solutions
 233 for shear stress, pore pressure, and normal stress change at the slip surface ($y \rightarrow 0^\pm$)
 234 in the Fourier-Laplace domain. In the Laplace-Fourier transform domain, we obtain the
 235 following relationships between change in shear stress $\bar{\hat{\tau}}'$, pore pressure change on either
 236 side of the layer $\bar{\hat{p}}^\pm$, and change in total normal stress $\bar{\hat{\sigma}}_{yy}$ in terms of $\bar{\hat{\delta}}_x$, $\bar{\hat{\delta}}_y$, and $\bar{\hat{p}}_c$:

$$\bar{\hat{\tau}}' = -\frac{G|k|\bar{\hat{\delta}}_x}{2(1-\nu_u)} \bar{H}_1(s, k) \quad (13)$$

237 and

$$\bar{p}^{\pm} = \mp \frac{ikGB\bar{\delta}_x}{3} \frac{1 + \nu_u}{1 - \nu_u} \bar{H}_2(s, k) - \bar{p}_c \frac{\mathcal{F}}{\mathcal{F} + 1} (\bar{H}_2(s, k) - 1) + \frac{|k|GB\bar{\delta}_y}{3} \frac{1 + \nu_u}{1 - \nu_u} \bar{H}_2(s, k), \quad (14)$$

238 and

$$\bar{\sigma}_{yy} = \bar{p}_c \frac{2}{3B(1 + \nu_u)} \frac{\mathcal{F}}{\mathcal{F} + 1} (\bar{H}_1(s, k) - 1) - \frac{G|k|\bar{\delta}_y}{2(1 - \nu_u)} \bar{H}_1(s, k), \quad (15)$$

239 where

$$\bar{H}_1(s, k) = 1 - \frac{2(\nu_u - \nu)}{1 - \nu} \frac{ck^2}{s} \frac{1 + \mathcal{F}}{\mathcal{F} + \sqrt{1 + s/ck^2}} \left(\sqrt{1 + s/ck^2} - 1 \right), \quad (16)$$

240 and

$$\bar{H}_2(s, k) = \frac{\sqrt{1 + s/ck^2} - 1}{\sqrt{1 + s/ck^2} + \mathcal{F}}. \quad (17)$$

241 \mathcal{F} is a dimensionless group that characterizes the importance of flux across the fault:

$$\mathcal{F} = \frac{\kappa_c}{\kappa} \frac{1}{|k|\epsilon}. \quad (18)$$

242 **2.2 Solutions to slip and pore pressure changes in Fourier-Laplace do-** 243 **main: Anti-plane shear**

244 Having solved the more complex in-plane shear problem, we may deduce the sim-
 245 pler anti-plane shear case. We note:

- 246 1. Any term of Eqs. (13), (14), and (15) that is linear in \bar{p}_c and $\bar{\delta}_y$ must be unchanged
 247 from the in-plane case, since these terms do not depend on fault-parallel slip.
- 248 2. Any term of Eqs. (13), (14), and (15) that is linear in $\bar{\delta}_x$ must be represented by
 249 the corresponding elastic anti-plane slip relationship, since anti-plane slip induces
 250 no volumetric stress and thus does not induce instantaneous or transient pore pres-
 251 sure response.

252 We thus arrive at the corresponding anti-plane shear relationships. We have:

$$\bar{\tau}' = -\frac{G|k|\bar{\delta}_x}{2}, \quad (19)$$

253 as was identified by Rice and Ruina (1983); Rice et al. (2001). Further, we find:

$$\bar{p}^\pm = -\bar{p}_c \frac{\mathcal{F}}{\mathcal{F}+1} (\bar{H}_2(s, k) - 1) + \frac{|k|GB\bar{\delta}_y}{3} \frac{1+\nu_u}{1-\nu_u} \bar{H}_2(s, k) \quad (20)$$

254 and

$$\bar{\sigma}_{yy} = \bar{p}_c \frac{2}{3B(1+\nu_u)} \frac{\mathcal{F}}{\mathcal{F}+1} (\bar{H}_1(s, k) - 1) - \frac{G|k|\bar{\delta}_y}{2(1-\nu_u)} \bar{H}_1(s, k), \quad (21)$$

255 where changes in normal stress σ_{yy} are identical to the in-plane case. It may seem sur-
 256 prising that the relationships above for anti-plane shear depend on Poisson's ratios (all
 257 except (19), the slip to shear stress relationship). However, the terms with Poisson's ra-
 258 tio are not stress components that arise from sliding, but rather ones that result from
 259 pressurization of the layer and dilation/compaction of the layer. The terms that depend
 260 on $\bar{\delta}_y$ represent mode I contribution of the interface deformation and terms with p_c rep-
 261 resent contributions from the pressure change at the interface. These contributions do
 262 not depend on the primary mode of sliding and are thus the same for the in-plane and
 263 anti-plane cases.

264 **3 Constitutive relations for a thin layer**

265 Here we describe the center pore pressure change p_c and the layer-perpendicular
 266 displacements δ_y in terms of the slip δ_x .

267 **3.1 Frictional constitutive law**

268 First, we consider the force balance within the layer:

$$\frac{\tau(x, t)}{\sigma(x, t) - p(x, y, t)} = f(x, y, t) \quad \text{for } -\epsilon < y < \epsilon, \quad (22)$$

269 where τ and σ are the shear stress and the effective normal stress in absence of pore pres-
 270 sure perturbations, respectively. Thus $\sigma = \sigma_0 + \sigma_{yy}$, where σ_0 is the total effective nor-
 271 mal stress at equilibrium, when there are no perturbations present in stresses or pore-
 272 pressure. The effective normal stress at equilibrium (σ_0) is thus the difference between
 273 the total ambient equilibrium normal stress and the ambient equilibrium pore-pressure,

274 but these two scalars are always combined in σ_0 . We emphasize that perturbations in
 275 pore-pressure are not written as a part of σ , while the ambient background pore-pressure
 276 is included in σ as a part of σ_0 . Similarly $\tau = \tau_0 + \tau'$ where τ_0 is the absolute equilib-
 277 rium shear stress and τ' represents any perturbations in shear stress from slip, pore-pressure
 278 or from external loading. The subscript $_0$ refers to a later assumption where we consider
 279 the system to be in equilibrium at $t = 0$ (see section 3.4).

280 We assume that τ and σ are constant with respect to y in the layer because the
 281 layer is thin. This assumption also implies that inertia can be ignored in the layer (Rice
 282 et al., 2014). f describes the frictional resistance at each point in the layer and p is the
 283 pore pressure perturbation assumed to follow the linear pressure distribution in equa-
 284 tion (11). In order to obtain the approximate frictional resistance of the entire layer, we
 285 average with respect to y using equation (11):

$$\tau \frac{(p_c - p^+) \log\left(\frac{\sigma - p^-}{\sigma - p_c}\right) + (p_c - p^-) \log\left(\frac{\sigma - p^+}{\sigma - p_c}\right)}{2(p_c - p^-)(p_c - p^+)} = \langle f \rangle, \quad (23)$$

286 where now all fields depend on x and t (not written explicitly for compactness), but not
 287 on y within the layer.

288 We assume that the layer-averaged frictional resistance is described by the rate-and-
 289 state friction law (e.g., Dieterich, 1979; Ruina, 1983; Marone, 1998):

$$\langle f \rangle = \frac{1}{2\epsilon} \int_{-\epsilon}^{\epsilon} f(x, y, t) dy = f_0 + a \log\left(\frac{V}{V_0}\right) + b \log\left(\frac{V_0 \theta}{L}\right), \quad (24)$$

290 where a is a constitutive parameter that weights the rate dependence of friction under
 291 constant state (also called the direct effect) and b is a constitutive parameter that weights
 292 the state dependence of friction at constant slip rate. V thus represents the slip rate of
 293 one side of the shear zone layer relative to the other, or in other words the integrated
 294 shear strain rate across the layer. L is the characteristics slip distance over which the
 295 state θ evolves. A mathematical definition of θ is offered later in the section where we
 296 introduce the state evolution law. In order to maintain consistency with the linearized
 297 stability analysis, discussed and presented in section 3.4, we select the nominal coeffi-
 298 cient of friction $f_0 = \tau_0/\sigma_0$ and the nominal slip speed as V_0 as the values at time $t =$
 299 0 , and the nominal state $\theta_0 = L/V_0$ as the steady-state value at time $t = 0$.

300 Equation (22) is non-linear, both in terms of strength dependence on pore-pressure
 301 and the coefficient of friction in equation (24). The linearization of the friction coeffi-
 302 cient is addressed in section 3.4. Here, we present the linearization with respect to small
 303 changes in pore pressure, to provide a more intuitive expression than equation 23. The
 304 linearization renders:

$$\tau = \tau_0 + \tau'(t) = (\sigma_0 + \sigma_{yy}(t) - \langle p(t) \rangle) \left[f_0 + a \log \left(\frac{V}{V_0} \right) + b \log \left(\frac{V_0 \theta}{L} \right) \right], \quad (25)$$

305 where the relevant average pore pressure $\langle p \rangle$ in the layer can be written as:

$$\langle p \rangle = \frac{1}{2\epsilon} \int_{-\epsilon}^{\epsilon} p(y) dy = \frac{1}{2} \left(p_c + \frac{p^+ + p^-}{2} \right). \quad (26)$$

306 Hence we conclude that, given our assumptions, we can simply use the average pres-
 307 sure in the layer as the relevant pore pressure in computing the effective normal stress
 308 in computing the shear resistance. As a reminder, our assumptions include the linear pore
 309 pressure distribution within the shear layer, the averaging of frictional strength described
 310 earlier in this section, and considering changes in pore pressure that are small compared
 311 to σ .

312 We note that the average pore pressure in the (distributed) shearing layer that we
 313 use in this study may not be a universally valid approach. In the presence of a thin low-
 314 permeability structure surrounding or next to the shearing layer, as typical for a fault
 315 core, the relevant pore pressure may be different (Jha & Juanes, 2014; Heimisson et al.,
 316 2019). Such structures are expected to be significant in well-developed fault zones (Caine
 317 et al., 1996). Our view could be most appropriate for less developed faults and labora-
 318 tory settings where the shear zone represents simulated gouge, or scenarios where the
 319 fault core may not generate a significant permeability contrast or flow barrier with the
 320 shear zone and/or the surrounding rock.

321 Furthermore, the localization of slip in fluid-saturated thin granular layers of dis-
 322 tributed shear is not fully understood at present and may require explicit modeling. If
 323 an ongoing localization process occurs, we also expect the relevant pore pressure to evolve
 324 in a complex way that requires explicit modeling. For example, studies indicate that, as
 325 instability develops, a localization process occurs and a distributed shear layer may col-
 326 lapse to a much narrower slip "surface" with the width of the order of several microns

327 (Rice et al., 2014; Platt et al., 2014). We expect that the relevant effective normal stress
 328 for shear resistance would then be determined by the pore pressure over that localized
 329 shear surface.

330 Equation (25) requires an equation for the evolution of the state variable θ , for ex-
 331 ample, the aging law:

$$\frac{d\theta}{dt} = 1 - \frac{\theta V}{L} - \frac{\alpha_{LD}\theta}{b\sigma} \dot{\sigma} \quad (27)$$

332 or the slip law (Ruina, 1983) These state evolution laws are identical when linearized around
 333 steady state slip and our analysis encompasses both (see section 3.4). Here, we have in-
 334 cluded the correction of Linker and Dieterich (1992) for the dependence of state on nor-
 335 mal stress. This dependence is proportional to the empirical Linker and Dieterich (1992)
 336 constant α_{LD} , which is typically between 0 and 0.5, but always less than f_0 .

337 **3.2 Constitutive equations for pore pressure in the layer**

338 Now we derive an evolution equation for the average pore pressure in the layer. Fol-
 339 lowing Segall and Rice (1995), the fluid mass conservation in the layer requires:

$$\frac{\partial m}{\partial t} + \frac{\partial q}{\partial y} = 0, \quad (28)$$

340 where m is the fluid mass content and q is the fluid mass flux. This expression consid-
 341 ers the fluid mass flux along the layer (along x) to be negligible, which is valid if flux along
 342 y dominates over flux along x . One obvious example is if the mobility or permeability
 343 in y direction is much larger than in the x direction. However, we expect this to hold
 344 more generally since the flux along y is proportional to $1/\epsilon$ but the flux along x is pro-
 345 portional to k and $\epsilon k \ll 1 \Rightarrow k \ll 1/\epsilon$. Nevertheless, this also depends on the rela-
 346 tion between the permeability of the host rock and permeability of the shear layer. If
 347 the host-rock is impermeable (or has low permeability compared to the one along the
 348 shear layer) then the flux along x cannot be ignored. The assumption that shear zone
 349 flux only occurs in fault normal direction is commonly applied in studies of thermal pres-
 350 surization (e.g., Rice, 2006; Bizzarri & Cocco, 2006).

351 We write $m = \rho_f n$, where ρ_f is the fluid density and $n = n^e + n^p$ is the sum of
 352 the elastic and plastic void volumes. Taking the time derivative of m yields

$$\dot{m} = \dot{\rho}_f n + \rho_f \dot{n}. \quad (29)$$

353 We now propose linearized relationships for the elastic void compressibility $\dot{n}^e = \phi(\beta_n^p \dot{p} -$
 354 $\beta_n^\sigma \dot{\sigma})$ and $\dot{\rho}_f = \rho_{fo}(\beta_f^p \dot{p} + \beta_f^\sigma \dot{\sigma})$, where β_f^p and β_n^p are fluid and elastic void compress-
 355 ibilities, respectively. Superscript p on β_f^p or β_n^p refers to “pressure” and specifies that
 356 this compressibility is defined under isotropic volumetric stress or pressure. Superscript
 357 σ on β_f^σ or β_n^σ refers to normal stress, specifically here σ_{yy} , and specifies that this com-
 358 pressibility is defined under uniaxial compressive or tensile stress. For example, for a lin-
 359 ear elastic solid, $\beta^p = 1/K$, where K is the bulk modulus. However $\beta^\sigma = (1+\nu)/(3K(1-$
 360 $\nu))$, which is the so called P-wave modulus. For $\nu = 0.25$, we find $\beta^\sigma = 5\beta^p/9$. We
 361 assume that $\sigma > 0$ reflects increased compression, or the compression positive conven-
 362 tion. Thus increased normal stress reduces the void-volume and decreases the fluid mass
 363 in each control volume. We refer the reader to Cocco and Rice (2002) for the detailed
 364 discussion of isotropic and uniaxial compressibilities in a poroelastic solid. The reference
 365 compressibilities are defined at the reference void fraction ϕ , which we interpret as poros-
 366 ity, and reference fluid density ρ_{fo} . Further, we assume that the plastic void fraction is
 367 equal to the plastic porosity: $n^{pl} = \phi^{pl}$, where the superscript “ pl ” refers to “plastic”.
 368 Thus, we arrive at:

$$\dot{m} = \rho_{fo}\phi(\beta_f^p \dot{p} + \beta_f^\sigma \dot{\sigma}) + \rho_{fo}\phi(\beta_n^p \dot{p} - \beta_n^\sigma \dot{\sigma} + \dot{\phi}^{pl}/\phi). \quad (30)$$

369 Combining equations (28) and (30) and integrating over the shear layer yields:

$$2\epsilon\rho_{fo}\phi \left[(\beta_f^p + \beta_n^p)\langle \dot{p} \rangle + (\beta_f^\sigma - \beta_n^\sigma)\dot{\sigma} + \langle \dot{\phi} \rangle^{pl}/\phi \right] + q^+ - q^- = 0, \quad (31)$$

370 Inserting the expressions for the fluid mass flux given a linear pressure distribution (equa-
 371 tions (10) and (11)) provides:

$$\langle \dot{p} \rangle + \frac{\beta_f^\sigma - \beta_n^\sigma}{\beta_f^p + \beta_n^p} \dot{\sigma} = -\frac{\langle \dot{\phi} \rangle^{pl}}{\phi(\beta_f^p + \beta_n^p)} + \frac{\kappa_c}{\epsilon^2\phi(\beta_f^p + \beta_n^p)} \left(\frac{1}{2}(p^+ + p^-) - p_c \right). \quad (32)$$

372 We have thus arrived at an evolution equation that relates normal stress (uniform
 373 over the layer) with average pore pressure and dilatancy, where the source of pore pres-
 374 sure stems from inelastic changes in porosity ϕ^{pl} . Segall and Rice (1995) and Segall et
 375 al. (2010) proposed that the inelastic porosity is a function of the state $\phi^{pl}(\theta)$. This idea

376 has been further observationally supported by Proctor et al. (2020). We assume that the
 377 state variable description of the plastic porosity changes reflects the average porosity change
 378 in the shear layer:

$$\langle \phi \rangle^{pl} = \langle \phi_0 \rangle^{pl} - \gamma \log \left(\frac{V_0 \theta}{L} \right), \quad (33)$$

379 where γ is a dilatancy coefficient usually taken as $\gamma \sim 10^{-4}$. The rate of change of the
 380 inelastic porosity is then given by:

$$\langle \dot{\phi} \rangle^{pl} = -\frac{\gamma}{\theta} \dot{\theta}. \quad (34)$$

381 It may be useful to summarize, at this stage, the treatment of porosity in the study.
 382 If the fault is loaded at rate V_0 and is also slipping at steady state everywhere at V_0 , which
 383 is a fundamental assumption of the stability analysis, then the porosity is simply ϕ that
 384 is the reference porosity. This means that here the initial value of the plastic porosity
 385 in equation (33) is $\langle \phi_0 \rangle^{pl} = 0$. The total porosity is then $\phi + \phi(\beta_n^p p - \beta_n^\sigma \sigma) + \langle \phi \rangle^{pl}$,
 386 where the second term is the elastic changes in porosity. We note that often equation
 387 (33) is written to describe the sum of reference porosity plus plastic porosity (e.g. Segall
 388 & Rice, 1995; Segall et al., 2010), which can be obtained by replacing $\langle \phi_0 \rangle^{pl} = \phi_0$. How-
 389 ever, here we have, for completeness introduced a separate value for the initial plastic
 390 porosity since in general the reference porosity may not be the same as the initial ref-
 391 erence plus plastic porosity.

392 **3.3 Fault-normal displacements of the shear layer**

393 We now seek a relationship that describes fault normal expansion or contraction
 394 of a thin gouge layer $\delta_y = u_y(y = \epsilon) - u_y(y = -\epsilon)$. We start by stating the conserva-
 395 tion of gouge mass, m_g , per unit volume:

$$\frac{\partial m_g}{\partial t} + \frac{\partial}{\partial y} ((1-n)\rho_g \dot{u}_y) + \frac{\partial}{\partial x} ((1-n)\rho_g \dot{u}_x) = 0, \quad (35)$$

396 where ρ_g is the gouge density; note that this is not the bulk density but the density of
 397 non-porous and intact gouge mass, that is the solid constituent of the gouge with all pores
 398 removed. Deformation u_x and u_y here refer to the internal deformation field of the gouge.
 399 Unlike the deformation of the bulk, in the gouge u_x and u_y are representing large strain

400 and non-elastic deformation. Here we have included the $\partial/\partial x$ term for completeness, but
 401 we will neglect assuming symmetry across the shear zone, as is discussed later. Now $m_g =$
 402 $(1 - n)\rho_g$ and thus:

$$\dot{m}_g = -\rho_g \dot{n} + (1 - n)\dot{\rho}_g. \quad (36)$$

403 Following the same arguments as in the previous section, we arrive at a linearized rela-
 404 tionship:

$$\dot{m}_g \approx -\rho_{g0}\phi(\beta_n^p \dot{p} - \beta_n^\sigma \dot{\sigma} + \dot{\phi}^{pl}/\phi) + (1 - \phi)\rho_{g0}(\beta_g^p \dot{p} + \beta_g^\sigma \dot{\sigma}), \quad (37)$$

405 where now β_g is the compressibility of the intact and non-porous gouge material and again
 406 superscript p and σ refer to the isotropic and uniaxial compressibilities, respectively.

407 Inserting Eq. 37 in Eq. 35 and integrating over the shear layer provides a relation-
 408 ship between dilatancy, pressure, and normal stress changes and gouge fault normal dis-
 409 placements:

$$\dot{\delta}_y = 2\epsilon \left(\frac{\phi}{1 - \phi} \beta_n^p - \beta_g^p \right) \left[\langle \dot{p} \rangle - \frac{\left(\frac{\phi}{1 - \phi} \beta_n^\sigma + \beta_g^\sigma \right)}{\left(\frac{\phi}{1 - \phi} \beta_n^p - \beta_g^p \right)} \dot{\sigma} \right] + 2\epsilon \frac{\langle \dot{\phi} \rangle^{pl}}{1 - \phi}. \quad (38)$$

410 If we assume that, at time $t = 0$, the fault is in a pressure equilibrium and sliding at
 411 steady state, the equation can be integrated trivially:

$$\delta_y = 2\epsilon \left(\frac{\phi}{1 - \phi} \beta_n^p - \beta_g^p \right) \left[\langle p \rangle - \frac{\left(\frac{\phi}{1 - \phi} \beta_n^\sigma + \beta_g^\sigma \right)}{\left(\frac{\phi}{1 - \phi} \beta_n^p - \beta_g^p \right)} \sigma \right] + 2\epsilon \frac{\langle \phi \rangle^{pl}}{1 - \phi}. \quad (39)$$

412 Where we have assumed that the average of \dot{u}_x with respect to y over the layer thick-
 413 ness is zero such that the x flux term in equation (35) is essentially neglected. This may
 414 be justified by assuming that internal deformation of the shear layer with respect to $y =$
 415 0 is anti-symmetric. This is likely if one side of the fault slips the same amount as the
 416 other, which is usually the case for symmetric geometries. We entrust the analysis of what
 417 might occur if such symmetry is not present to future work.

418 3.4 Linearized stability analysis

419 We now seek to analyze the stability of the steady shear (or sliding) in the layer
 420 to small perturbations. If the perturbation is small, the friction law and other consti-
 421 tutive relationship can be linearized around the initial steady-state configuration. We
 422 seek a solution to the linearized form (Rice et al., 2001) of the friction law and state evo-
 423 lution (Eqs. 25 and 27, respectively) as well as the linearized equation describing the time-
 424 evolution of the layer pressure p_c (Eq. 32). We carry out the stability analysis in the joint
 425 Laplace-Fourier transform domain (Eq. 12), which is equivalent to seeking a solution to
 426 the linearized system of equation for a slip perturbation $\delta_x = e^{st+ikx}$, which is applied
 427 at $t = 0$ (e.g., Rice et al., 2001).

428 The goal of the linearized stability analysis is to obtain the characteristic equation
 429 where we can solve for s as a function of $k = 2\pi/\lambda$, where λ is wavelength, and other
 430 parameters. If the solution has $\Re(s(k)) > 0$, then the steady-state sliding is linearly un-
 431 stable to the perturbations with corresponding wavenumbers, whereas if $\Re(s(k)) < 0$,
 432 the sliding is stable and the perturbations decay exponentially. If $\Re(s(k)) = 0$ pertur-
 433 bations neither grow nor decay; in this case we refer to k as the critical wavenumber k_{cr} ,
 434 which thus defines a length-scale at which development of instabilities is possible. This
 435 important wavenumber is discussed in more detail in Section 4.

436 We note that the sign of k when it refers to a Fourier-mode perturbation in slip
 437 applied to the fault simply reflects the direction of the slip wave as it travels along the
 438 interface. The symmetry of the problem indicates that there is no inherent dependence
 439 on the wave directionality. Indeed, the term with the opposite sign in p^+ and p^- (equa-
 440 tion 14), which implies the directionality dependence (as was discussed by Heimisson et
 441 al. (2019)), cancels when computing $\langle p \rangle$.

442 Stability analysis of frictional sliding is more commonly done, and perhaps more
 443 widely known, in the the context of simpler system where this bulk response is neglected.
 444 That is a single degree-of-freedom system commonly referred to as the spring-block slider
 445 (e.g. Ruina, 1983; Segall & Rice, 1995; Segall et al., 2010). In this case, the goal is to
 446 derive a critical stiffness of the spring, defined as stress drop per unit slip. The spring
 447 stiffness is also commonly represented by the symbol k , but here we shall denote it as
 448 \mathcal{K} and thus the critical spring stiffness as \mathcal{K}_{cr} . If $\mathcal{K} > \mathcal{K}_{cr}$ then instabilities do not de-
 449 velop at steady-state sliding, but if $\mathcal{K} < \mathcal{K}_{cr}$ instabilities can be generated from small

450 perturbations at steady state. In applying the spring-slider analysis to fault stability, which
 451 are not uniform in space, the argument is made that the spring stiffness represents a crack
 452 stiffness in an elastic medium and the spring stiffness can be replaced with the scaling
 453 $\mathcal{K}_{cr} \sim G/L_{cr}$, with L_{cr} being a critical crack length, or half crack length. For quasi-
 454 static elastic medium this substitution provides the correct scaling such that $k_{cr} = 2\pi/\lambda_{cr} \sim$
 455 $1/L_{cr}$ with the only difference being an order 1 constant factor (Rice et al., 2001). How-
 456 ever, if transient bulk response, which depends on the wavenumber, plays a role in the
 457 stability, such as in an elastodynamic solid (Rice et al., 2001), or poroelasticity (see Heimisson
 458 et al. (2019) and this study) this simple correspondence between spring-slider and con-
 459 tinuum bulk analysis does not hold anymore in a general sense.

460 The linearized form of Eqs. 25 and 27 around steady state sliding can be expressed
 461 (Rice et al., 2001):

$$\frac{d}{dt}\tau'(t) = -\frac{a\sigma_0}{V_0}\frac{dV}{dt}(f_0 - \alpha_{LD})\frac{d}{dt}(\sigma_{yy} + p) - \frac{V_0}{L}\left[\tau_0 + \tau'(t) - f_0(\sigma_0 - \sigma_{yy} - p) - \frac{(a-b)\sigma_0}{V_0}(V - V_0)\right], \quad (40)$$

462 Transforming in the Laplace-Fourier domain renders (Heimisson et al., 2019):

$$\left(s + \frac{V_0}{L}\right)\bar{\tau}' = -\left[f_0\left(s + \frac{V_0}{L}\right) - \alpha_{LD}s\right](\bar{\sigma}_{yy} + \bar{p}) + \left[\frac{a\sigma_0}{V_0}s^2 + \frac{(a-b)\sigma_0}{L}s\right]\bar{\delta}_x. \quad (41)$$

463 Expressions for $\bar{\tau}'$ and $\bar{\sigma}_{yy}$ are provided in Eqs 13 and 15, but we note the introduction
 464 of the minus sign in front of $\bar{\sigma}_{yy}$ due to a change in sign convention since the equation
 465 describing friction considers tensile stress to be negative. As previously discussed, the
 466 value chosen for the relevant pore pressure within the layer is open to some interpreta-
 467 tion but here we take the average value as in Eq. 26.

468 Now we seek to eliminate the eigenfunction $\bar{\delta}_x$ from the equation above and retrieve
 469 the characteristic equation. However, we first need to derive linear relationships such that
 470 $\bar{p}_c \propto \bar{\delta}_x$ and $\bar{\delta}_y \propto \bar{\delta}_x$.

471 Let $\langle\phi^{pl}\rangle = \phi_0 + \Delta\phi_p$, $\theta = L/V_0 + \Delta\theta$, and $V = V_0 + \Delta V$ where Δ indicates a
 472 small perturbation around the steady state value, with the latter being the first term on
 473 the right hand side of each equation. Inserting into Eq. 34 and carrying out a lineariza-
 474 tion around steady state provides the following expression for $\Delta\dot{\phi}^{pl}$ and the correspond-
 475 ing Laplace transform

$$\Delta \dot{\phi}^{pl} = -\frac{\gamma V_0}{L} \Delta \dot{\theta} \Rightarrow \mathcal{L}(\Delta \dot{\phi}^{pl}) = \overline{\Delta \dot{\phi}^{pl}} = -\frac{\gamma V_0 s}{L} \overline{\Delta \theta}. \quad (42)$$

476 From Segall and Rice (1995), we have a linearized state evolution law (see also Ruina,
477 1983):

$$\Delta \dot{\theta} = -\frac{V_0}{L} \Delta \theta - \frac{\Delta V}{V_0} \quad (43)$$

478 and the Laplace transform renders

$$\overline{\Delta \theta} = -\frac{s \bar{\delta}_x}{V_0 (s + \frac{V_0}{L})}. \quad (44)$$

479 Thus the linear relationship between plastic changes in porosity (or alternatively inelas-
480 tic dilatancy or compaction) is

$$\overline{\Delta \phi}^{pl} = \frac{\gamma}{L} \frac{s \bar{\delta}_x}{(s + \frac{V_0}{L})}, \quad (45)$$

481 where we interpret the relationship as the average representing the plastic changes in poros-
482 ity within the shear zone.

483 Applying the Laplace transform to Eq. 32 and substituting Eq 45 yields

$$\langle \bar{p} \rangle = \frac{1}{2} \left(\bar{p}_c + \frac{\bar{p}^+ + \bar{p}^-}{2} \right) = -\frac{\gamma}{\beta L} \frac{s}{s + \frac{V_0}{L}} \bar{\delta}_x + \frac{\kappa_c}{2\beta \epsilon^2 s} (\bar{p}^+ - 2\bar{p}_c + \bar{p}^-), \quad (46)$$

484 Further substitution of Eq. 14 then provides one linear relationship between \bar{p}_c , $\bar{\delta}_y$, and
485 $\bar{\delta}_x$. However, another constitutive relationship is needed to eliminate both \bar{p}_c and $\bar{\delta}_y$. This
486 relationship comes from Eq. 39 by taking the Laplace transform and substituting Eq.
487 45:

$$\bar{\delta}_y = 2\epsilon \left(\frac{\phi}{1-\phi} \beta_n^p - \beta_g^p \right) \left[\frac{1}{2} \left(\bar{p}_c + \frac{\bar{p}^+ + \bar{p}^-}{2} \right) - \frac{\left(\frac{\phi}{1-\phi} \beta_n^\sigma + \beta_g^\sigma \right)}{\left(\frac{\phi}{1-\phi} \beta_n^p - \beta_g^p \right)} \bar{\sigma}_{yy} \right] + \frac{2\epsilon}{1-\phi} \frac{\gamma}{L} \frac{s \bar{\delta}_x}{(s + \frac{V_0}{L})}. \quad (47)$$

488 Then through substitution of Eqs. 14 and 15 for the in-plane case, or Eqs. 20 and 21 for
489 the anti-plane case, we obtain another linear relationship between \bar{p}_c , $\bar{\delta}_y$, and $\bar{\delta}_x$.

490 This means that the linear relationship between stress or pore pressure and \bar{p}_c , $\bar{\delta}_y$,
491 and $\bar{\delta}_x$ in Eqs. 13, 14, and 15 for in-plane, or Eqs. 19, 20, and 21 for anti-plane can all

492 be expressed only in terms of $\bar{\delta}_x$. Then substitutions of those expressions into the char-
 493 acteristic equation (41) allows for elimination of $\bar{\delta}_x$ and provides finally two equations
 494 that can be solved numerically for $s(k)$. The two equations are obtained by requiring that
 495 both the real part and imaginary part of the characteristic equation are zero (e.g., Rice
 496 et al., 2001; Heimisson et al., 2019). We do not present here the full characteristic equa-
 497 tion due to the complexity of the expression, but provide a Matlab code where it is im-
 498 plemented and can be solved (see Acknowledgments). Numerical exploration of the char-
 499 acteristic equation would suggest no more than two roots (within numerical precision).
 500 These roots have the same real part and imaginary part except the latter changing sign.
 501 However, due to the presence of half-integer terms and the sheer size of the expression,
 502 determining analytically the number of roots has not been feasible. In the next section,
 503 we discuss some approximation and implications as well as show numerical solutions.

504 **4 Times scales and approximations to the critical wavenumber**

505 Let us present the results on the stability of steady-state sliding of a dilating shear
 506 layer embedded into and coupled with a poroelastic solid. Much of this discussion fo-
 507 cuses either on approximate expressions for the critical wavenumber, or solving the char-
 508 acteristic equation numerically using a standard root finding algorithm.

509 The critical wavenumber $k_{cr} = 2\pi/\lambda_{cr}$ represents the wavenumber at the bound-
 510 ary between stable and unstable sliding. The critical wavenumber marks the point of a
 511 Hopf bifucation where $\text{Re}(s(k_{cr})) = 0$ but $\text{Im}(s(k_{cr})) \neq 0$ in general. A small-magnitude
 512 perturbation in slip with a larger wavenumber ($k > k_{cr}$), or alternatively a smaller wave-
 513 length, would decay exponentially. However, a perturbation in slip of a smaller wavenum-
 514 ber than k_{cr} ($k < k_{cr}$), or alternatively larger wavelength, would grow and may nucle-
 515 ate a seismic event. A Fourier-mode perturbation with exactly $k = k_{cr}$ would simply
 516 oscillate with a fixed frequency and neither grow nor decay.

517 In the following sections, we present approximations to the critical wavenumber in
 518 certain limiting cases. To obtain these approximate expressions, we carry out following
 519 steps.

- 520 1. We introduce s' and k' , which are non-dimensional versions of s and k and are ob-
 521 tained by substitution $s = s'V_0/L$ and $k = k'k_{cr}^{anti}$, where $k_{cr}^{anti} = 2\sigma_0(b-a)/(GL)$
 522 is the critical wavenumber for quasi-static, anti-plane sliding between two elastic

523 solids (Rice et al., 2001). This quantity is of the same order as the correspond-
 524 ing in-plane sliding wavenumber (Rice et al., 2001) but does not depend on Pois-
 525 son’s ratio, which can be either drained or undrained. This non-dimensionalization
 526 implies that s' and k' are generally of order unity near critical stability.

- 527 2. We introduce a non-dimensional half-thickness ϵ' of the shear layer, by substitu-
 528 tion $\epsilon = \epsilon'/k_{cr}^{anti}$. Since a fundamental assumption of the analysis is that $k\epsilon \ll$
 529 1, we may use ϵ' as a small parameter in which the characteristic equation can be
 530 expanded.
- 531 3. We carry out a Taylor expansion of both the real and imaginary parts of the char-
 532 acteristic equation. We retain terms up to first order in ϵ' . We also explore the
 533 leading-order terms that are proportional to $1/\kappa_c$ if appropriate. These terms are
 534 retained because they become large if κ_c is small and thus may provide insight into
 535 transitional regimes at low shear-zone mobility.

536 4.1 Characteristic time scales

537 In order to obtain insight into the role of diffusion in the stability of the frictional
 538 interface, we start by analyzing the time scales involved as perturbations grow around
 539 steady state sliding. The problem has three characteristic time scales. First, a frictional
 540 nucleation time scale:

$$t_{nu} = \frac{L}{V_0}, \quad (48)$$

541 which is a natural time-scale for the evolution of the frictional state and scales how fast
 542 instabilities nucleate or decay back to steady state sliding in a stable regime. Further,
 543 it offers a first-order approximation to the instability time of sources above steady state
 544 in the spring-slider analysis (Heimisson & Segall, 2018).

Second, we investigate the time scale of diffusion into the bulk:

$$t_b = \frac{1}{ck^2}. \quad (49)$$

Lastly, a time scale of flux in the shear layer:

$$t_f = \frac{1}{\mathcal{F}^2 ck^2} = \frac{\kappa^2 \epsilon^2}{\kappa_c^2 c} = \frac{c\epsilon^2}{M^2 \kappa_c^2}, \quad (50)$$

545 where the last equality is obtained by the substitution $\kappa = c/M$, which is the relation-
 546 ship between the mobility and hydraulic diffusivity in a linear poroelastic bulk.

From these time scales, we identify two non-dimensional time scales. First,

$$\mathcal{T}_f = \frac{t_{nu}}{t_f} = \frac{LM^2\kappa_c^2}{V_0c\epsilon^2}, \quad (51)$$

547 where \mathcal{T}_f represents the ratio of the time scale of nucleation to the time scale of flux through
 548 the shear layer. If \mathcal{T}_f is small compared to unity than nucleation occurs much faster than
 549 the fluid flux in the shear layer. Since such flux is needed to minimize the effects of di-
 550 lational stabilization, we expect that a small value of \mathcal{T}_f corresponds to the limit where
 551 dilatancy is important. On the other hand, if \mathcal{T}_f is large, then nucleation occurs over a
 552 longer time than the flux and dilatancy can be ignored.

553 The second non-dimensional time scale is $t_{nu}/t_b = Lck^2/V_0$, however, we substi-
 554 tute $k \rightarrow k_{cr}^{anti}$ since it is not convenient to express the non-dimensional time scale ex-
 555 plicitly in terms of k , which is treated as a variable in the characteristic equation. We
 556 thus obtain a non-dimensional time scale independent of k :

$$\mathcal{T}_b = \frac{4c\sigma_0^2(b-a)^2}{V_0G^2L}, \quad (52)$$

557 which is valid as long as the critical wavenumber is of the same order as k_{cr}^{anti} . When
 558 \mathcal{T}_b is small compared to unity we may effectively ignore the fluid diffusion in the bulk
 559 on the time scale of nucleation and we expect undrained bulk response. However, if \mathcal{T}_b
 560 is large then fluid in the bulk can diffuse at the time scale of nucleation and the bulk re-
 561 sponse is drained. For $\mathcal{T}_b \sim 1$, we expect transient poroelastic response of the bulk.

562 The two non-dimensional time scales here share several parameters, notably the
 563 hydraulic diffusivity of the host rock c . Moving forward, we shall investigate different
 564 limits of stability by systematically changing either \mathcal{T}_f or \mathcal{T}_b while keeping the other pa-
 565 rameter constant.

566 4.2 Limit of $\kappa_c \rightarrow 0$

567 Let us analyze a simple limit where the permeability or mobility of the shear layer
 568 is zero, in addition to assuming that the bulk response is either drained or undrained.
 569 In this limit, as $\epsilon \rightarrow 0$, one can show , for in-plane sliding, that:

$$|k_{cr}| \simeq k_{cr}^{un} \left(1 - \frac{f_0\gamma}{\beta\sigma_0(b-a)} + \mathcal{O}(\epsilon) \right), \quad (53)$$

570 where

$$k_{cr}^{un} = k_{cr}^{anti}(1 - \nu_u) = \frac{2\sigma_0(b-a)(1 - \nu_u)}{GL} \quad (54)$$

571 is the critical wavenumber for the corresponding elastic problem of in-plane sliding as-
 572 suming an undrained Poisson's ratio. We present k_{cr} within an absolute value to reflect
 573 that it can be both positive and negative depending on the directionality of the slip wave
 574 as was previously discussed. This also implies that, if the right hand side of the equaion
 575 is negative, then clearly the critical wavenumber does not exist.

576 Similarly, for drained bulk response

$$|k_{cr}| \simeq k_{cr}^d \left(1 - \frac{f_0\gamma}{\beta\sigma_0(b-a)} + \mathcal{O}(\epsilon) \right), \quad (55)$$

577 where

$$k_{cr}^d = k_{cr}^{anti}(1 - \nu) = \frac{2\sigma_0(b-a)(1 - \nu)}{GL} \quad (56)$$

578 is similarly the drained elastic critical wavenumber of in-plane sliding.

579 For anti-plane sliding, there is no difference in the bulk response at drained or undrained
 580 condition (to zeroth order in ϵ') and the corresponding limit is simply

$$|k_{cr}| \simeq k_{cr}^{anti} \left(1 - \frac{f_0\gamma}{\beta\sigma_0(b-a)} + \mathcal{O}(\epsilon) \right), \quad (57)$$

581 We thus observe that the dilatancy has a primary effect on the critical wavenum-
 582 ber in this limit. Equations (53) and (57) are, in a sense, equivalent to the undrained
 583 limit identified by Segall and Rice (1995) with a single-degree-of-freedom spring-slider
 584 analysis, except equations (53) and (57) are for a deformable poroelastic bulk. However,
 585 equation (55) does not have a direct correspondence in the Segall and Rice (1995) anal-
 586 ysis. This is because the Segall and Rice (1995) analysis had effectively only one diffu-
 587 sion time controlled by the hydraulic diffusivity c of the bulk. Here, we consider that the
 588 time scale of flux within the shear layer may be very different (see Section 4.1). Thus
 589 this analysis adds to the findings of Segall and Rice (1995) by suggesting that, as long
 590 as the shear layer is sufficiently impermeable, then dilatancy stabilization can occur even
 591 in a highly diffusive surroundings.

592 The first-order correction for Eqs. (53) and (55) can be written out explicitly as:

$$\mathcal{O}(\epsilon) = \epsilon \frac{2f_0\gamma(f_0\gamma - (b-a)\phi\sigma_0(\beta_f^p + \beta_n^p))(\beta_g^p + \phi(\beta_f^p - \beta_g^p))(\beta_f^p - \beta_f^\sigma + \beta_n^p + \beta_n^\sigma)}{L\phi^2\sigma_0(\beta_f^p + \beta_n^p)^3(b-a)(1-\phi)}. \quad (58)$$

593 The corresponding anti-plane $\mathcal{O}(\epsilon)$ correction term in equation (57) is obtained by mul-
 594 tiplying the in-plane correction (equation 58) by $1/(1-\nu)$ and $1/(1-\nu_u)$ for the drained
 595 and undrained bulk responses, respectively.

596 This correction arises due to the shear-zone expansion from non-elastic porosity
 597 changes from dilatancy and elastic porosity changes due to pore pressure change and nor-
 598 mal stress changes. It is likely that the sign of this term is mostly governed by the sign
 599 of $f_0\gamma - (b-a)\phi\sigma_0(\beta_f^p + \beta_n^p) = f_0\gamma - (b-a)\sigma_0\beta$. Thus, if $f_0\gamma/((b-a)\sigma_0\beta) > 1$, this term
 600 would act to destabilize. However, $f_0\gamma/((b-a)\sigma_0\beta) = 1$ is the condition when Eqs.
 601 (53), (55), and (57) suggest no unstable wavenumbers, since $k_c = 0$ to the leading or-
 602 der. We thus conclude that, for sets of parameters where the interface is conditionally
 603 unstable due to small perturbations around steady state, fault-perpendicular displace-
 604 ments act to further stabilize sliding as $\kappa_c \rightarrow 0$.

605 4.3 Undrained bulk response ($c \rightarrow 0$)

606 In this particular limit, we neglect any diffusion of fluids in the bulk. However, we
 607 note that the shearing layer itself can equilibrate pore pressure, in other words, $\kappa_c >$
 608 0 . In this particular case, the characteristic equation is greatly simplified because $\bar{H}_1 \rightarrow$
 609 1 and $\bar{H}_2 \rightarrow 1$ by design (Heimisson et al., 2019). However the full solution to the sys-
 610 tem is still too complicated to provide any useful insight if written out as an equation.
 611 We thus approximate the characteristic equation following the procedure outlined be-
 612 fore. We obtain the following expression:

$$|k_{cr}| \simeq k_{cr}^{un} \frac{1}{1 + \mathcal{C}}, \quad (59)$$

613 where \mathcal{C} is a non-dimensional and non-negative parameter:

$$\mathcal{C} = \epsilon \frac{2f_0\gamma(3 - 2B(1 + \nu_u))}{3L(1 - \phi)} \quad (60)$$

614 The corresponding anti-plane limit is obtained by substitution of $k_{cr}^{un} \rightarrow k_{cr}^{anti}$ and
 615 $\mathcal{C} \rightarrow \mathcal{C}/(1 - \nu_u)$.

616 In the limit $\epsilon \rightarrow 0$, we clearly see that $k_{cr} = k_{cr}^{un}$ as is expected. It is notable that
 617 \mathcal{C} describes stabilization due to expansion of the gouge in response to inelastic dilatancy,
 618 which causes fault perpendicular displacements. The bracket $3 - 2B(1 + \nu_u) \geq 0$, since
 619 at most $B = 1$ and $\nu_u = 0.5$. This bracket characterizes the competition between two
 620 processes: increased compression of the shear layer due to expansion against the poro-
 621 elastic host rock and increased pore pressure in the shear layer due to the compression
 622 of the host rock. If $B = 1$, and the undrained Poisson's ratio of the host rock implies
 623 that it is nearly incompressible, the two effects cancel completely. We conclude that the
 624 influence of the shear layer expansion in the undrained bulk limit can be neglected as
 625 long as

$$\mathcal{C} = \epsilon \frac{2f_0\gamma(3 - 2B(1 + \nu_u))}{3L(1 - \phi)} \ll 1. \quad (61)$$

626 It is worth noting that higher order terms may become significant in the limit of
 627 $\kappa_c \rightarrow 0$. But, as we recognized in the previous section, the limit of $\kappa_c = 0$ gives rise
 628 to dilatancy stabilization of the zeroth order with respect to ϵ . By retaining the leading-
 629 order terms with dependence on $1/\kappa_c$, we find that, in order for equation (60) to be a
 630 valid approximation, one needs to have:

$$\epsilon^4 \frac{V_0^2 \beta f_0 \gamma}{4L^2 \kappa_c^2 a \sigma_0} \ll 1. \quad (62)$$

631 If the inequality is violated, we expect the onset of stabilization through dilatancy in the
 632 sense identified by Segall and Rice (1995).

633 **4.4 Drained bulk response ($c \rightarrow \infty$)**

634 In this limit, we assume that the bulk is highly diffusive on any time scale relevant
 635 to dilatancy and for the onset of instability. However, we assume that the shear layer
 636 pressure equilibrates on a finite time scale, i.e. $\kappa_c > 0$. We carry out the same proce-
 637 dure as for undrained bulk response to obtain an approximate expression for the crit-
 638 ical wavenumber:

$$|k_{cr}| \simeq k_{cr}^d \frac{1}{1 + \mathcal{C}_d}. \quad (63)$$

639 Curiously, this approximation has exactly the same form as for the undrained bulk with
 640 some slight changes:

$$k_{cr}^d = \frac{2\sigma_0(b-a)(1-\nu)}{GL} \quad (64)$$

641 and

$$\mathcal{C}_d = \epsilon \frac{2f_0\gamma}{L(1-\phi)}. \quad (65)$$

642 The corresponding anti-plane limit is obtained by substitution of $k_{cr}^d \rightarrow k_{cr}^{anti}$ and
 643 $\mathcal{C}_d \rightarrow \mathcal{C}_d/(1-\nu)$.

644 The critical wavenumber for the undrained bulk response (Eq. 59) can be turned
 645 into the one for the drained bulk response (Eq. 63) simply by substituting $\nu_u \rightarrow \nu$ and
 646 setting $B = 0$. The substitution of the undrained Poisson's ratio by the drained one
 647 is obviously relevant. The substitution of $B = 0$ is also easily explained since, for the
 648 fully drained bulk response, fault perpendicular movements do not induce an increased
 649 pore pressure adjacent to the shear zone.

650 It is worth noting that the only compressibility that shows up in Eq. 59 and Eq.
 651 63 is $\beta = \phi(\beta_f^p + \beta_n^p)$ (defined in the same way as by (Segall & Rice, 1995)). All other
 652 compressibilities, such as those related to uniaxial compression or the fault gouge com-
 653 pressibilities, influence the solution through higher-order terms that are neglected here,
 654 which indicates that the other compressibilities are not as important.

655 In the drained bulk limit, a violation of inequality (62) also indicates the onset of
 656 traditional dilatancy stabilization as in Segall and Rice (1995).

657 **5 Results**

658 In the results section we solve the characteristic equation using a standard root-
 659 finding algorithm. We focus on two parameter regimes for bulk and poroelastic prop-
 660 erties: a Westerly Granite with $B = 0.81$, $\nu = 0.25$, $\nu_u = 0.33$ and a Ohio sandstone
 661 with $B = 0.50$, $\nu = 0.18$, and $\nu_u = 0.28$, both under in-plane and anti-plane sliding.

662 We selected Westerly Granites since it is commonly used in various rock mechanics ex-
663 periments. The Ohio Sandstone values were then picked to give an example of a ma-
664 terial with significantly different poroelastic constants. These values are taken from the
665 poroelastic material parameters for rocks listed in Cheng (2016) (see also references therein).

666 In addition to exploring the granite and sandstone, we also explore two limits - a
667 thinner shear layer with $\epsilon = 1$ mm and a thicker shear layer with $\epsilon = 10$ cm - which
668 would reveal differences corresponding to the fault-normal displacement stabilization pro-
669 cess. Other chosen parameters are listed in the Appendix (table A1).

670 **5.1 In-plane shear**

671 We first investigate the case of in-plane sliding which gives rise to more variabil-
672 ity in the drained and undrained limits and better highlights the different regimes pre-
673 viously discussed.

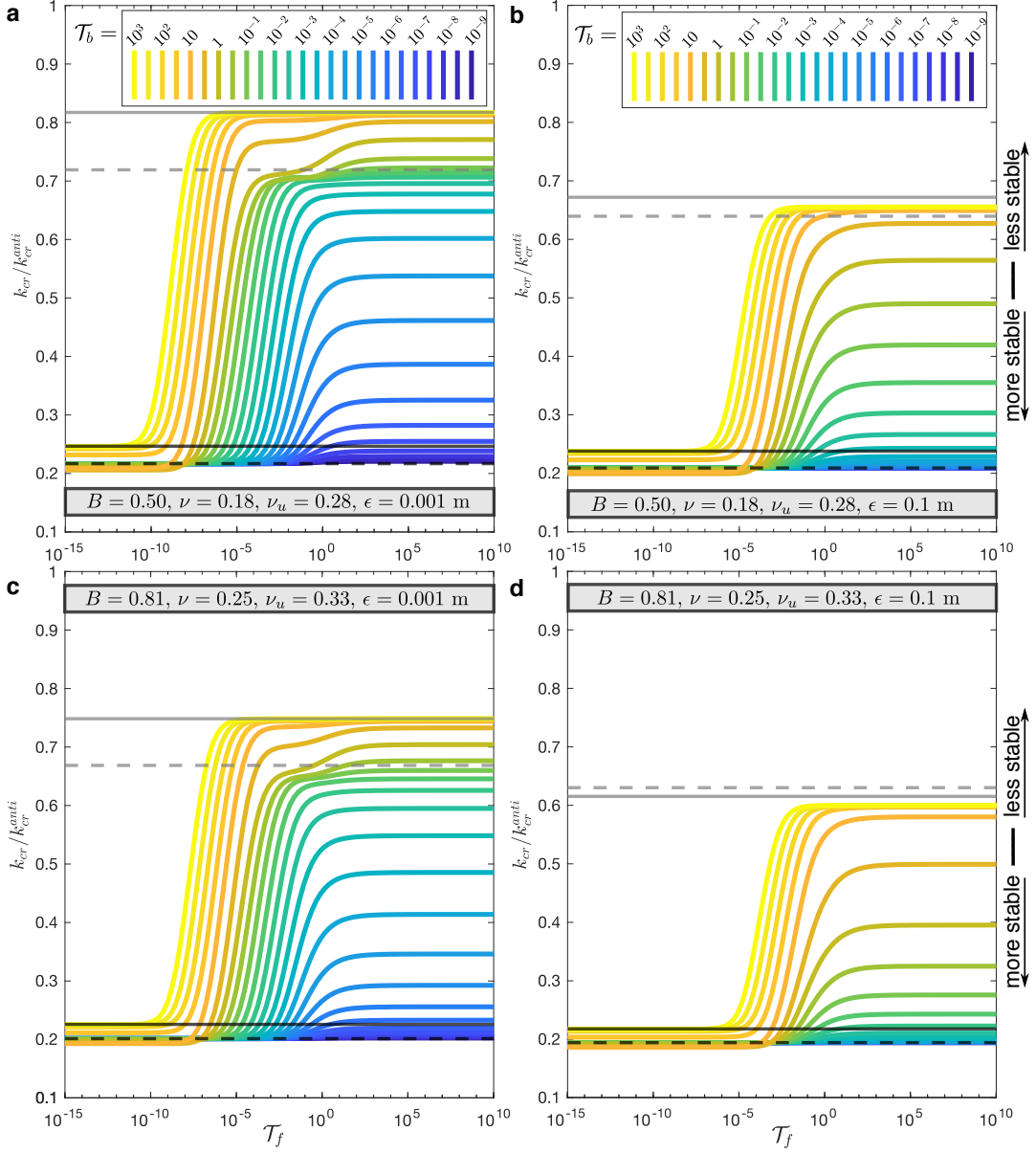


Figure 2. Changes in critical wavenumber k_{cr} , non-dimensionalized by k_{cr}^{anti} , when varying \mathcal{T}_f and keeping \mathcal{T}_b fixed at various values, for in-plane shear. The limit of the undrained bulk and $\kappa_c = 0$ (equation 53) is shown by black dashed line. The limit of the drained bulk and $\kappa_c = 0$ (equation 55) is shown by the black solid line. The dashed and solid grey lines indicate the results for the undrained and drained bulk, respectively, with the leading-order ϵ correction (equations 59 and 63). **a** Ohio Sandstone and thinner shear zone. **b** Ohio Sandstone and thicker shear zone. **c** Westerly Granite and thinner shear zone. **d** Westerly Granite and thicker shear zone. We generally observe that the numerical solution coincides with the relevant analytical estimates obtained, although, the estimate for the undrained bulk with the leading order ϵ correction only works well for the thinner shear zones.

674 Figure 2 illustrates how varying the non-dimensional flux time scale \mathcal{T}_f while fix-
 675 ing the non-dimensional bulk-diffusion time scale \mathcal{T}_b alters the critical wavenumber. Gen-
 676 erally, a low flux time scale, for example due to low permeability of the shear zone, trans-
 677 lates into more stabilized slip since dilatancy of the shear zone can increase the effective
 678 normal stress and increase the frictional resistance. However, this effect is not only con-
 679 trolled by the time scale of shear-zone flux, because a more diffusive bulk will limit the
 680 range at which dilatancy can stabilize sliding. However, in the extreme limit that the
 681 bulk diffusion is very fast, but shear zone flux is very small, dilatancy can still stabilize.
 682 See, for example, the bright yellow line in Figure 2 or dark blue line in Figure 3. How-
 683 ever, this limit is less stable than when both \mathcal{T}_f and \mathcal{T}_b are small, since the bulk response
 684 is drained and thus has effectively a lower Poisson’s ratio.

685 We clearly observe that the analytical estimates of section 4.2 derived for the limit
 686 of $\kappa_c = 0$ for drained and undrained bulk response generally hold in all cases when solv-
 687 ing the complete characteristic equation (Figures 2 and 3, black solid and dashed lines).
 688 Similarly we see good agreement in the case of a thicker shear zone (panels b and d) where
 689 the critical wavenumber is further reduced as a consequence of fault-normal displacements.
 690 In the limit of drained bulk response and high flux (grey solid line) there is significantly
 691 stabilization compared to the thinner shear zone, but the first-order correction shows some
 692 mismatch in these cases (panels b and d in Figures 2 and 3), indicating that higher-order
 693 terms are becoming important, as would be expected for a wider shear layer. We observe
 694 that the curious limit of high-flux but undrained bulk response (grey dashed line) is not
 695 an actual limiting case, but rather describes an intermediate stability characteristic in
 696 a certain parameter range for the thinner shear layer (panels a and c). This is not sur-
 697 prising, since the two time scales, \mathcal{T}_f and \mathcal{T}_b , are not independent, in the sense that the
 698 flux time scale also depends on the hydraulic diffusivity of the bulk. Thus a limit where
 699 the bulk can be considered undrained but the flux time scale is fast can only approxi-
 700 mately hold over a certain range of time scales. This intermediate stability character-
 701 istics of high-flux but undrained bulk response (grey dashed line) shows up quite clearly
 702 in the cases of a thinner shear zone (Figures 2 and 3, a and c) as clustering or bending
 703 of the plotted lines.

704 For the thicker shear layer (Figures 2 and 3, panels b and d), we find substantial
 705 stabilization in comparison with the thinner shear layer especially in the limit of high
 706 flux and high bulk diffusivity (grey solid lines), which occurs due to the fault-normal dis-

707 placements from dilatancy and the associated increase in normal stress on the shearing
 708 layer. Since this effect occurs even in the drained limit, it would also be predicted if the
 709 bulk were modeled as simple elastic material.

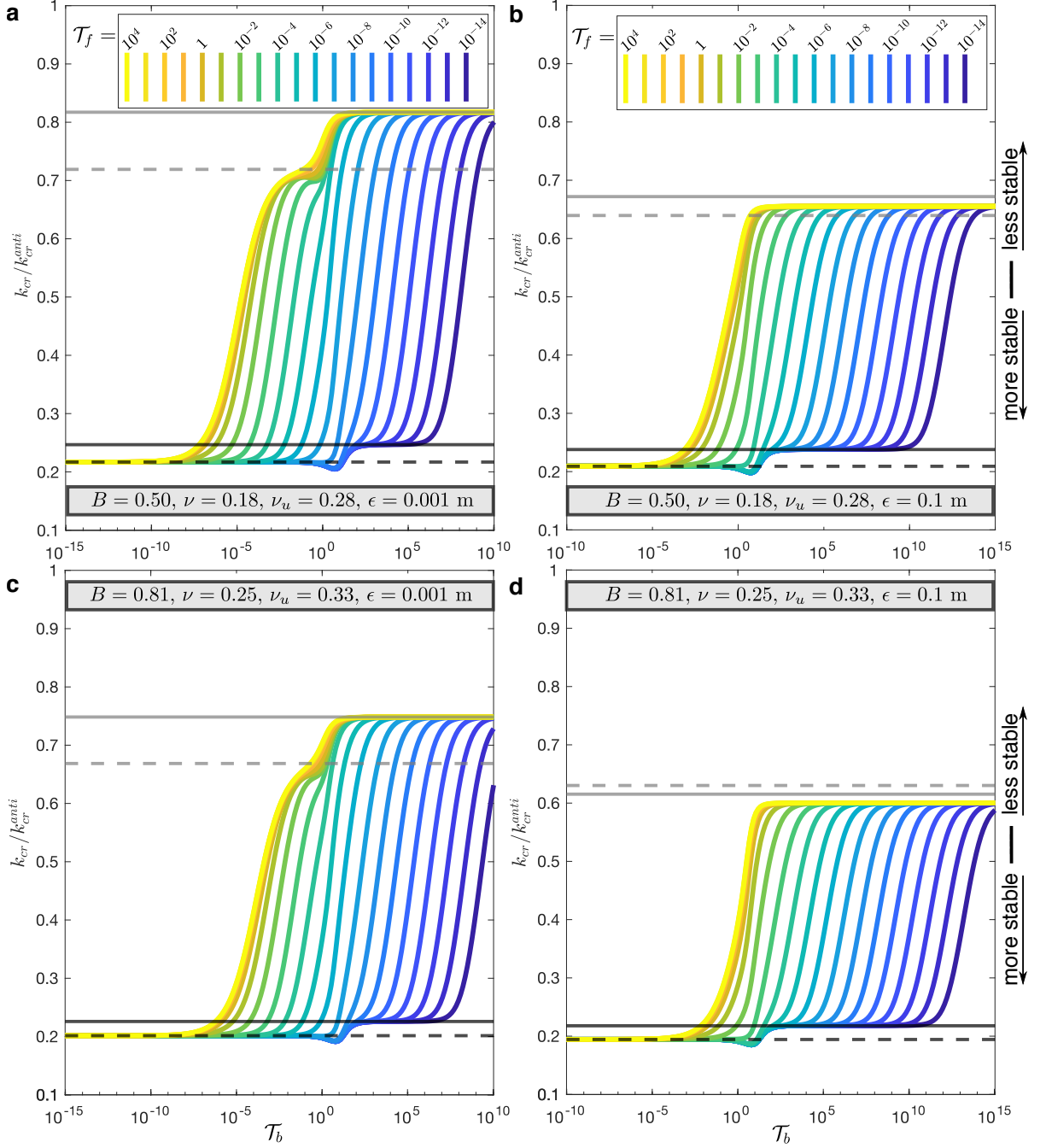


Figure 3. Changes in critical wavenumber k_{cr} , non-dimensionalized by k_{cr}^{anti} , when varying \mathcal{T}_b but keeping \mathcal{T}_f fixed, for in-plane shear. Definitions of lines and panels are the same as in Figure

2.

710 It is notable that under in-plane sliding the lowest possible critical wavenumber,
711 or the highest degree of stability at steady state, is not in limit where \mathcal{T}_f and \mathcal{T}_b are both
712 small, or completely undrained limit. It can be seen clearly in Figure 3, that at near $\mathcal{T}_b \sim$
713 1 certain lines have a dimple going below black dashed line. Since this occurs $\mathcal{T}_b \sim 1$
714 and, as we will see in the following subsection, does not occur for the anti-plane sliding,
715 we conclude that this additional stabilization occurs due to a transient poroelastic re-
716 sponse of the bulk.

717 **5.2 Anti-plane sliding**

718 Here we explore the stability of the steady state for anti-plane sliding. Since equa-
719 tion 19 has no dependence on Poisson's ratio and no transient poroelastic response, we
720 observe much less variability in stability in the explored limiting cases than for the in-
721 plane sliding.

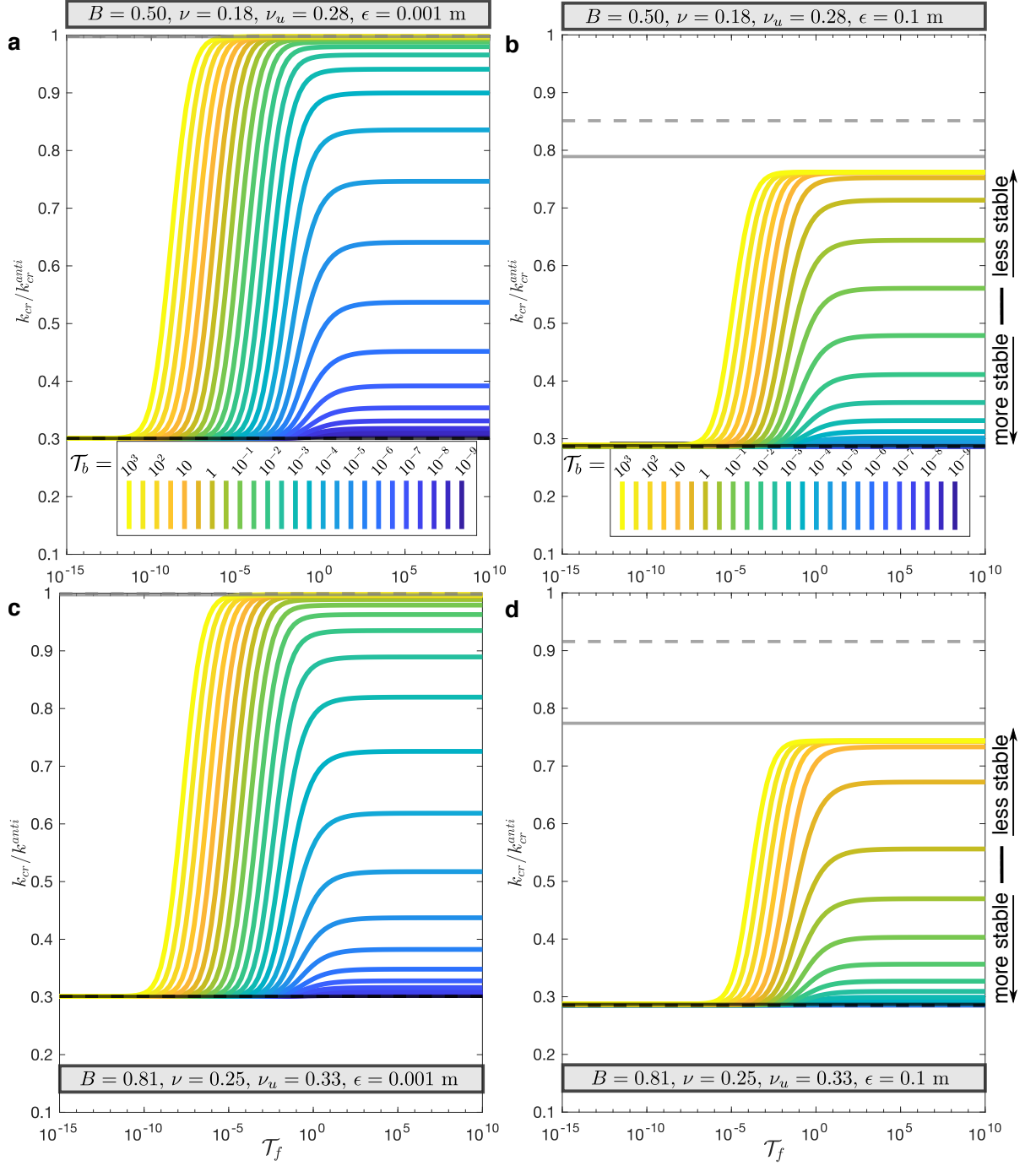


Figure 4. Changes in critical wavenumber k_{cr} , non-dimensionalized by k_{cr}^{anti} , when varying \mathcal{T}_f but keeping \mathcal{T}_b fixed, for anti-plane sliding. The black dashed line indicates an estimate of the critical wavenumber for the limit of the undrained bulk and $\kappa_c = 0$. Black solid line represents the critical wavenumber for drained bulk and $\kappa_c = 0$ limit (equation 57). Grey dashed line represents results for the undrained bulk with leading order ϵ correction (see equation 59 and following text). Solid grey line is the drained bulk with leading order ϵ correction (see equation 63 and following text). **a** Ohio Sandstone and thinner shear zone. **b** Ohio Sandstone and thicker shear zone. **c** Westerly Granite and thinner shear zone. **d** Westerly Granite and thicker shear zone.

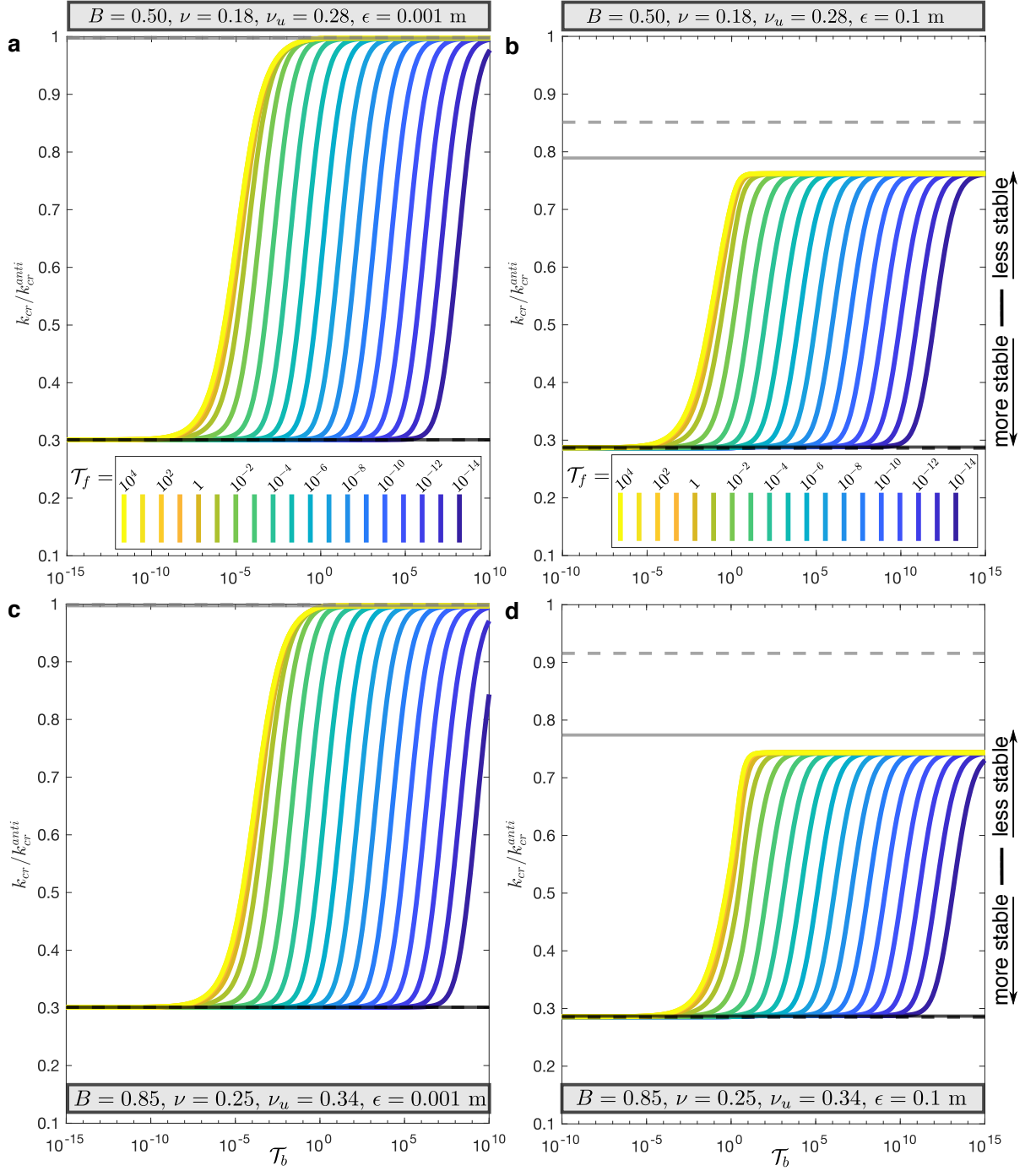


Figure 5. Changes in critical wavenumber k_{cr} , non-dimensionalized by k_{cr}^{anti} , when varying \mathcal{T}_b but keeping \mathcal{T}_f fixed, for anti-plane sliding. Definitions of lines and panels are the same as in Figure 4.

722 Figures 4 and 5 illustrate that, as expected, the anti-plane case is much simpler than
 723 the in-plane one. This is because dilatancy induced pore-pressure changes are dominat-
 724 ing the stability characteristic, but the drained and undrained bulk response in the anti-
 725 plane case is less significant and arises only from the differences in effective normal stress
 726 (equations 20 and 21), but not through the sliding-induced shear stress changes (equa-
 727 tion 19). However, these differences in drained and undrained bulk response are very small
 728 as can be seen by how the solid and dashed lines in Figures 4 and 5 (a and d) appear
 729 to be overlapping. This highlights that poroelasticity can play an important role through
 730 shear stress changes during rupture propagation or event nucleation, but only for in-plane
 731 sliding.

732 In general, all the same limits exist as for the in-plane case, except we do not ob-
 733 serve the intermediate stability characteristic for the undrained bulk with high flux (grey
 734 dashed line), furthermore, we do not observe the increased stability beyond the fully undrained
 735 limit around near $\mathcal{T}_b \sim 1$ (e.g., Figure 3). However, many similarities remain, for ex-
 736 ample, we see that that in the anti-plane case, much like the in-plane case, dilatancy in-
 737 duced pore-pressure changes are possible even if the bulk is highly diffusive, as long as
 738 the shear zone flux is sufficiently low. Further, we see that stability is for anti-plane is
 739 also characterized by the competition of time-scales: \mathcal{T}_b and \mathcal{T}_f , where if one is large the
 740 stability can still be changed dramatically by making the other sufficiently small. The
 741 presence of this competition or interaction of time scales, in both in-plane and anti-plane
 742 sliding, suggests that problems involving fluid interactions with frictional sliding may be
 743 lacking important insights if they are simplified to a problem with a single diffusion time.
 744 Further, it stands to reason that if the problem has more diffusional timescales than \mathcal{T}_b
 745 and \mathcal{T}_f the stability may be altered in unexpected ways.

746 6 Discussion

747 6.1 Comparison with Segall and Rice (1995)

748 This study is greatly influenced by the seminal work of Segall and Rice (1995), which
 749 showed that inelastic dilatancy can significantly stabilize sliding of a frictional interface.
 750 This theory has received particular notice since it offers a physical explanation for gener-
 751 ating slow slip events on faults (Segall et al., 2010). It is, therefore, worth summariz-

ing and highlighting some of the differences between the analysis presented here and the original analysis of Segall and Rice (1995).

The most fundamental difference between the stability analysis in Segall and Rice (1995) and in our study is the treatment of the bulk. We present the stability analysis in a fully coupled poroelastic medium, whereas Segall and Rice (1995) used a single-degree-of-freedom spring-slider representation of the bulk. Thus, instead of solving for a critical wavenumber (or wavelength) of a perturbation, they solved for the critical spring stiffness. Using elementary fracture mechanics for crack stiffness, one can interpret the spring-slider analysis in terms of the critical wavenumber (Dieterich, 1992). Indeed, our equation (57), for example, provides results completely consistent with the spring-slider analysis up to a scaling factor of order 1 and ignoring the $O(\epsilon)$ correction. However, other aspects of the stability determined in this study cannot be captured with the spring-slider analysis; for example, the transient stability regimes where neither drained nor undrained response dominates (Figures 2, 3, 4, and 5). Such regimes depend on the wavenumber (equation 49), which changes one of the relevant diffusion times, and thus cannot be captured by rescaling of the critical stiffness (e.g., equations 16 and 17). In Segall and Rice (1995), the transient stability regimes, controlled by a relevant diffusion time, do not depend on a length scale.

The second key difference is the presence of two time scales at which pressure equilibration occurs. These are the time scale of pressure equilibration through shear layer flux \mathcal{T}_f , and the time scale related to the diffusion through the bulk \mathcal{T}_b . Segall and Rice (1995) and the alternative diffusion model in Segall et al. (2010) only have one diffusion time scale. The analysis with two diffusion time scales provides additional insights into the problem. For example, there is a parameter range where the bulk diffusion can be extremely fast and the bulk response can be considered drained. However, the shear-layer flux time scale is sufficiently slow such that dilatancy can act to stabilize sliding by reducing pore pressure and increasing effective normal stress. That limit may be of important geological relevance. It has been frequently reported that the fault core, where shear localization occurs, has very low permeability (Caine et al., 1996; Wibberley & Shimamoto, 2003; Behnsen & Faulkner, 2011), while the adjacent damage zone is highly permeable (F. Chester & Logan, 1986; Mitchell & Faulkner, 2012).

783 The final key difference, which is also discussed in some detail in the following sub-
784 section, is that our study accounts for the fault-normal displacements that arise from di-
785 latancy and pressure changes in the shear zone. This effect was not considered by Segall
786 and Rice (1995), and it has not been studied previously in the fault mechanics literature
787 to the best of our knowledge. As has been shown here, this effect gives rise to a differ-
788 ent mechanism through which dilatancy can stabilize sliding.

789 **6.2 Fault-normal displacements**

790 Theoretical studies and field-based observations usually support the idea that seis-
791 mic slip in fault gouge occurs in an extremely localized shear layer of 1 – 100 μm . The
792 stability analysis and numerical simulations of Rice et al. (2014) and Platt et al. (2014)
793 used a thermo-poro-mechanical model and suggested that the width of a shear zone arises
794 as a competition between destabilizing thermal pressurization process and a stabilizing
795 process that may be dilatancy or rate-strengthening friction. In the absence of a stabi-
796 lizing process, the shear zone thickness becomes infinitesimal. Their findings are gener-
797 ally supported in field observations. For example, J. S. Chester et al. (2005) examined
798 the shear zone of the Punchbowl fault in California which has been exhumed from 2–
799 4 km depths and found the principal shear layer of 100-300 microns. De Paola et al. (2008)
800 examined cataclastic fault cores in the Northern Apennines and observed extreme shear
801 strain localization of some tens of microns. However, studies also suggest that the shear
802 layer can be wider. Boullier et al. (2009) examined two borehole cores, which intersected
803 the Chelungpu fault at about 1 km depth after the Chi-Chi earthquake in 1999. Their
804 analysis suggested thin shear localization zone from one core of 2 mm and the other 20
805 mm. While these widths are small compared to virtually all other characteristic dimen-
806 sions of that earthquake, it does suggest that even localization at seismic ruptures can
807 vary substantially.

808 In this study, we have focused on the stability around steady-state quasi-static (slow)
809 sliding. It is less clear how localized the shear zones are at creep rates in the range of
810 centimeters to millimeters per year. Laboratory experiments suggest that the width of
811 such localization depends on the normal stress, where a more delocalized shear-zone is
812 formed at low normal stress (Torabi et al., 2007). These observations beg the question
813 of how localized are the shear zones in regions of slow slip and tectonic tremor in sub-
814 duction zones. The same question applies to the roots of some strike-slip faults where

815 it has been suggested that pore pressure may be near lithostatic (e.g., Rubinstein et al.,
 816 2007; Thomas et al., 2009). It has recently been argued that tectonic mélanges, some
 817 hundreds of meters thick, may play an important role in aseismic slip processes along
 818 the subduction zone interface (Fagereng et al., 2018; Raimbourg et al., 2019). It is not
 819 clear if such large structures can be regarded as a single shear zone and would thus fall
 820 under the scope of our analysis. However, geological observations of mélanges strongly
 821 suggest that not all shear strain on faults occurs in extremely localized zones.

822 If the shear layers are sufficiently thick during quasi-static shear, as appears to be
 823 possible from lab and field observations, then they can generate fault-normal displace-
 824 ments that stabilize sliding. These displacements are largely caused by the same dila-
 825 tancy process that reduces pore pressure in the shear zone. The additional stabilization
 826 due to fault-normal displacements occurs because the shear layer must expand against
 827 the stiff host rock, where slip speed is increasing, and that increases the normal stress
 828 on the layer and hence its resistance to sliding. Similarly, where slip speed decreases, the
 829 shear zone compacts which reduces normal stress and resistance to sliding. This may also
 830 stabilize sliding since the reduced normal stress causes the perturbation in slip speed to
 831 decrease and tend to steady state and the reduced normal stress may prevent a local in-
 832 crease in shear stress on the fault. From equations 63 and 65, we can infer that
 833 if $\mathcal{C}_d = \epsilon 2f_0\gamma/L(1 - \phi)$ is order 1/10 then shear-zone expansion, in drained conditions,
 834 will produce significant stabilization due to shear-zone expansion. Since $2f_0/(1 - \phi)$ is
 835 typically order 1, we suggest that the shear zone thickness produces significant stabiliz-
 836 ing fault-normal displacements through dilatancy if $\epsilon \gtrsim 0.1L/\gamma$. Taking $L \sim 10 \mu\text{m}$
 837 and $\gamma \sim 10^{-4}$ indicates that the shear layer of the width $\epsilon \sim 1 \text{ cm}$ can be considered
 838 an approximate threshold at which fault-normal displacements are large enough to pro-
 839 duce a significant stabilizing effect. The same estimate is found for drained bulk (see equa-
 840 tion 61) if $(3 - 2B(1 + \nu_u)) \sim 1$, which is typically true.

841 We hypothesize that, during shear localization, the fault-normal motion may de-
 842 lay or perhaps prevent further localization, since a perturbation, which otherwise could
 843 induce an instability process with extreme localization, may be stabilized by the (larger)
 844 shear-zone width at that time. Note that the conclusions may be different for other as-
 845 sumptions of the relevant pore pressure values within the fault zone, such as taking the
 846 largest value of pore fluid pressure, which would promote localization. Other factors not
 847 considered in this study may affect shear localization, such as thermal pressurization of

848 pore fluids considered in Rice et al. (2014) and Platt et al. (2014). However, since the
849 effects of thermal pressurization on the nucleation process is not likely until late in the
850 nucleation process (Segall & Rice, 2006), which is also when inertial effects are impor-
851 tant and our analysis would not be valid.

852 **7 Conclusions**

853 The stabilizing effect of dilatancy on slip along a frictional fault has garnered in-
854 terest since the mechanism was proposed and formulated by Segall and Rice (1995) within
855 the scope of the rate-and-state friction framework. While a number of studies have im-
856 plemented dilatancy in simulations of slow and fast slip on faults with rate-and-state fric-
857 tion, the implementation and formulation of dilatancy in a fully-coupled poroelastic solid
858 has been missing. Here we present a closed system of equation describing a shearing gouge
859 layer under in-plane and anti-plane loading with rate-and-state dependent friction and
860 undergoing state-dependent dilatancy/compaction.

861 We have presented a linearized analysis of the stability of shearing in the layer around
862 steady state. We have identified two mechanisms through which dilatancy can stabilize
863 frictional sliding: first, by reducing pore pressure in the shearing layer and second, by
864 expanding the layer and generating fault-normal displacements in the bulk. The former
865 mechanism was identified by Segall and Rice (1995), where they show that it is most ef-
866 fective for an undrained bulk with loss of stabilization as the bulk response approaches
867 the drained limit. We add to this criterion by highlighting that such stabilization can
868 occur even if the bulk is highly diffusive and responds in a drained manner, due to lower
869 flux within the shear layer. The latter mechanism, due to fault-normal displacements,
870 has not been identified previously, to the best of our knowledge. It primarily results from
871 dilatancy-induced expansion of the shear zone. The expanding shear zone presses against
872 the host rock and increases normal stress acting on the shear zone, thus increasing fric-
873 tional resistance. This effect does not require the presence of pore pressure changes and
874 occurs even if the shear zone and bulk responses are drained.

875 The results of this study highlight the importance of considering the realistic hydro-
876 mechanical structure of faults around the thin shear layers, including the actual width
877 of the shearing layer as well as the potential difference between the hydraulic diffusiv-
878 ity of the shear layer (which is thin but finite) and the surrounding host rock. The iden-

879 tified stability properties near steady-state sliding will inform future numerical explo-
 880 rations of the full non-linear problem of a shear fault sliding with dilatancy/compaction
 881 in a poroelastic solid.

882 **Acknowledgments**

883 This study was supported by the Geophysics Option Postdoctoral Fellowship from the
 884 Division of Geological and Planetary Sciences at Caltech to E.R.H. and by the NSF-IUCRC
 885 Center for Geomechanics and Mitigation of Geohazards (projects GMG-4.1, GMG-4.2)
 886 to N.L. We thank reviewers Allan Rubin and Massimo Cocco for their constructive re-
 887 marks and we thank Paul Segall for helpful comments. This is a theoretical paper and
 888 contains no data. Code for determining the critical stability and solving equation 41, which
 889 also contains explicit expressions for equations too long to write out in this paper, is found
 890 here

891 <https://doi.org/10.5281/zenodo.5005276> (see Heimisson, 2021)

892 **Appendix A Parameter values**

893 Here we discuss the parameters that are kept constant when we numerically solve
 894 for the roots of the characteristic equations at critical stability, as shown in Figures 2,
 895 3, 4, and 5. These parameters and their values are summarized in Table A1.

896 The material parameters that are fixed are the shear modulus G of the bulk, var-
 897 ious compressibilities of the gouge, and the reference porosity of the gouge at steady state
 898 sliding ϕ_0 , which is assumed to be equivalent to the reference void volume per unit vol-
 899 ume. We use $G = 30$ GPa which is selected somewhat arbitrarily but which is a com-
 900 mon value used for crustal rocks and should be applicable to well-packed fault gouge.
 901 The other bulk poroelastic parameters are varied and explained in the main text. It is
 902 worth noting that, to explore different values of the non-dimensional parameter \mathcal{T}_f in
 903 Figures 2, 3, 4, and 5 we only change κ_c but, to explore different values of \mathcal{T}_b , we change
 904 both the hydraulic diffusivity of the bulk and κ_c so that \mathcal{T}_f is fixed (since it depends on
 905 both c and κ_c), in accordance with equations 52 and 51.

906 In selecting the various gouge material properties, we broadly follow Segall and Rice
 907 (1995), Rice et al. (2014), and Platt et al. (2014) where appropriate. We take $\beta_f^p = 0.44 \cdot$
 908 10^{-9} Pa $^{-1}$ (Fine & Millero, 1973). We use $\beta_n^p = 6.0 \cdot 10^{-9}$ Pa $^{-1}$ which Rice et al. (2014)

909 and Platt et al. (2014) inferred to be appropriate for damaged rocks based on the data
 910 by Wibberley and Shimamoto (2003) and using the analysis of Rice (2006). The com-
 911 pressibility of the gouge grains, β_g^p , has not, to the best of our knowledge, been featured
 912 in previous literature. We expect this compressibility to be low compared to the fluid
 913 or pore compressibilities. We simply assume that it is the inverse of a typical rock bulk
 914 modulus of 50 GPa, that is, $\beta_g^p = 0.02 \cdot 10^{-9} \text{ Pa}^{-1}$. The uniaxial compressibilities β_f^σ ,
 915 β_n^σ , and β_g^σ have not received much attention in the previous literature. Here we assume
 916 that we can obtain the uniaxial compressibility by multiplying the isotropic compressibil-
 917 ity by a factor of 5/9. As discussed in the main text, this is only strictly true for a lin-
 918 ear elastic material. However, this likely offers a reasonable correspondence between isotropic
 919 and uniaxial compressibility more generally. Nevertheless, we suggest that more stud-
 920 ies are needed to determine if uniaxial compressibilities can be vastly different from the
 921 isotropic compressibilities. We select the reference porosity at steady-state sliding, also
 922 interpreted as the void volume per unit volume, as $\phi = 0.068$. This is a commonly used
 923 value based on Wibberley and Shimamoto (2003). Finally, we follow Segall and Rice (1995)
 924 in their modeling of the Marone et al. (1990) experiments and select the dilatancy co-
 925 efficient as $\gamma = 1.7 \cdot 10^{-4}$.

926 For the friction and fault loading parameters, we select fairly standard values (Ta-
 927 ble A1) frequently used in the literature. It is worth mentioning that, for simplicity, we
 928 have taken the Linker and Dieterich (1992) constant $\alpha_{LD} = 0$, which implies no explicit
 929 dependence of the state variable on normal stress changes. This essentially means that
 930 we consider the effective normal stress changes to be gradual enough that the shear stress
 931 stays proportional to the effective normal stress, a reasonable assumption given the slow
 932 slip considered. In Table A1, we provide both initial shear and normal stress for conve-
 933 nience, but the two are not independent due to the condition that the fault is initially
 934 at steady state and are related through $\tau_0 = f_0 \sigma_0$.

935 Throughout the main text, we have mostly used G , B , ν , ν_u , c to fully describe the
 936 poroelastic bulk properties. However, in a few cases, we have used different set of pa-
 937 rameter for compactness, that is, M , α , and κ . Here we list a few relationships that would
 938 allow the reader to convert between these parameter sets:

$$B = \frac{3M\alpha(1 - 2\nu)}{2G(1 + \nu) + 3M\alpha^2(1 - 2\nu)}$$

Table A1. Parameters that are kept constant in the study

Symbol	Description	Value
<i>Bulk and gouge material properties</i>		
G	Shear modulus	30 GPa
$\beta_f^p, \beta_f^\sigma$	Isotropic and uniaxial fluid compressibility	$0.44 \cdot 10^{-9} \text{ Pa}^{-1}$, $0.24 \cdot 10^{-9} \text{ Pa}^{-1}$,
$\beta_n^p, \beta_n^\sigma$	Isotropic and uniaxial pore volume compressibility	$6.0 \cdot 10^{-9} \text{ Pa}^{-1}$, $3.3 \cdot 10^{-9} \text{ Pa}^{-1}$,
$\beta_g^p, \beta_g^\sigma$	Isotropic and uniaxial solid gouge compressibility	$0.020 \cdot 10^{-9} \text{ Pa}^{-1}$, $0.011 \cdot 10^{-9} \text{ Pa}^{-1}$,
ϕ_0	Reference porosity	0.068
<i>Friction and loading parameters</i>		
L	Characteristic state evolution distance	100 μm
a	Direct rate dependence of friction	0.01
b	State dependence of friction	0.02
α_{LD}	Linker and Dieterich (1992) constant	0.0
V_0	Steady-state and reference sliding velocity	10^{-9} m/s
f_0	Steady-state coefficient of friction at V_0	0.6
τ_0	Initial shear stress	20.0 MPa
σ_0	Initial effective normal stress	33.3 MPa

$$\nu_u = \frac{2G\nu + M\alpha^2(1 - 2\nu)}{2G + 2M\alpha^2(1 - 2\nu)}$$

$$B = \frac{3(\nu_u - \nu)}{\alpha(1 - 2\nu)(1 + \nu_u)}$$

$$c = M\kappa.$$

References

- 939
- 940 Behnsen, J., & Faulkner, D. (2011). Water and argon permeability of phyllosilicate
941 powders under medium to high pressure. *Earth Planet. Sc. Lett.*, *116*(B12).
- 942 Bhattacharya, P., & Viesca, R. C. (2019). Fluid-induced aseismic fault slip out-
943 paces pore-fluid migration. *Science*, *364*(6439), 464–468. doi: 10.1126/science
944 .aaw7354
- 945 Bizzarri, A., & Cocco, M. (2006). A thermal pressurization model for the sponta-
946 neous dynamic rupture propagation on a three-dimensional fault: 1. Method-
947 ological approach. *Journal of Geophysical Research: Solid Earth*, *111*(B5). doi:
948 <https://doi.org/10.1029/2005JB003862>
- 949 Boullier, A.-M., Yeh, E.-C., Boutareaud, S., Song, S.-R., & Tsai, C.-H. (2009). Mi-
950 croscale anatomy of the 1999 chi-chi earthquake fault zone. *Geochemistry,*
951 *Geophysics, Geosystems*, *10*(3). doi: 10.1029/2008GC002252
- 952 Brace, W. F., Paulding Jr., B. W., & Scholz, C. (1966). Dilatancy in the fracture of
953 crystalline rocks. *Journal of Geophysical Research (1896-1977)*, *71*(16), 3939-
954 3953. doi: <https://doi.org/10.1029/JZ071i016p03939>
- 955 Bürgmann, R. (2018). The geophysics, geology and mechanics of slow fault slip.
956 *Earth Planet. Sc. Lett.*, *495*, 112–134.
- 957 Caine, J. S., Evans, J. P., & Forster, C. B. (1996). Fault zone architecture and per-
958 meability structure. *Geology*, *24*(11), 1025–1028.
- 959 Cheng, A. H.-D. (2016). *Poroelasticity* (Vol. 877). Springer.
- 960 Chester, F., & Logan, J. M. (1986). Implications for mechanical properties of brit-
961 tle faults from observations of the punchbowl fault zone, california. *Pure Appl.*
962 *Geophys.*, *124*(1-2), 79–106.
- 963 Chester, F. M., Chester, J. S., Kirschner, D. L., Schulz, S. E., & Evans, J. P. (2004).
964 Structure of large-displacement, strike-slip fault zones in the brittle continental
965 crust. *Rheology and deformation in the lithosphere at continental margins*, *1*,
966 223–260.
- 967 Chester, F. M., Evans, J. P., & Biegel, R. L. (1993). Internal structure and weaken-
968 ing mechanisms of the san andreas fault. *J. Geophys. Res.*, *98*(B1), 771–786.
- 969 Chester, J. S., Chester, F. M., & Kronenberg, A. K. (2005). Fracture surface energy
970 of the punchbowl fault, san andreas system. *Nature*, *437*(7055), 133–136.
- 971 Ciardo, F., & Lecampion, B. (2019). Effect of dilatancy on the transition from

- 972 aseismic to seismic slip due to fluid injection in a fault. *Journal of Geophys-*
 973 *ical Research: Solid Earth*, 124(4), 3724–3743. doi: [https://doi.org/10.1029/](https://doi.org/10.1029/2018JB016636)
 974 2018JB016636
- 975 Cocco, M., & Rice, J. R. (2002). Pore pressure and poroelasticity effects in coulomb
 976 stress analysis of earthquake interactions. *Journal of Geophysical Research:*
 977 *Solid Earth*, 107(B2), ESE 2-1-ESE 2-17. doi: [https://doi.org/10.1029/](https://doi.org/10.1029/2000JB000138)
 978 2000JB000138
- 979 Dal Zilio, L., Lapusta, N., & Avouac, J.-P. (2020). Unraveling scaling prop-
 980 erties of slow-slip events. *Geophysical Research Letters*, 47(10). doi:
 981 10.1029/2020GL087477
- 982 De Paola, N., Collettini, C., Faulkner, D. R., & Trippetta, F. (2008). Fault zone
 983 architecture and deformation processes within evaporitic rocks in the upper
 984 crust. *Tectonics*, 27(4). doi: 10.1029/2007TC002230
- 985 Detournay, E., & Cheng, A. H.-D. (1995). Fundamentals of poroelasticity. In *Analy-*
 986 *sis and design methods* (pp. 113–171). Elsevier.
- 987 Dieterich, J. H. (1979). Modeling of rock friction: 1. experimental results and consti-
 988 tutive equations. *Journal of Geophysical Research: Solid Earth*, 84(B5), 2161-
 989 2168. doi: 10.1029/JB084iB05p02161
- 990 Dieterich, J. H. (1992). Earthquake nucleation on faults with rate-and state-
 991 dependent strength. *Tectonophysics*, 211(1), 115-134. doi: [https://doi.org/](https://doi.org/10.1016/0040-1951(92)90055-B)
 992 10.1016/0040-1951(92)90055-B
- 993 Dor, O., Rockwell, T. K., & Ben-Zion, Y. (2006, Mar 01). Geological observations
 994 of damage asymmetry in the structure of the San Jacinto, San Andreas and
 995 Punchbowl faults in Southern California: A possible indicator for preferred
 996 rupture propagation direction. *Pure Appl. Geophys.*, 163(2), 301–349. doi:
 997 10.1007/s00024-005-0023-9
- 998 Dunham, E. M., & Rice, J. R. (2008). Earthquake slip between dissimilar poroelas-
 999 tic materials. *J. Geophys. Res. Solid Earth*, 113(B9). (B09304) doi: 10.1029/
 1000 2007JB005405
- 1001 Ellsworth, W. L. (2013). Injection-induced earthquakes. *Science*, 341(6142),
 1002 1225942.
- 1003 Fagereng, Å., Diener, J. F., Ellis, S., & Remitti, F. (2018). *Fluid-related deformation*
 1004 *processes at the up-and down-dip limits of the subduction thrust seismogenic*

- 1005 *zone: What do the rocks tell us* (Vol. 534). Geol. Soc. Am. Spec. Pap.
- 1006 Ferdowsi, B., & Rubin, A. M. (2020). A granular physics-based view of fault fric-
 1007 tion experiments. *Journal of Geophysical Research: Solid Earth*, 125(6),
 1008 e2019JB019016. doi: <https://doi.org/10.1029/2019JB019016>
- 1009 Fine, R. A., & Millero, F. J. (1973). Compressibility of water as a function
 1010 of temperature and pressure. *The Journal of Chemical Physics*, 59(10),
 1011 5529-5536. Retrieved from <https://doi.org/10.1063/1.1679903> doi:
 1012 10.1063/1.1679903
- 1013 Heimisson, E. R. (2021, June). *eliasrh/Poroelastic.linear.stability: Release for pub-*
 1014 *lication of Heimisson, Rudnicki, and Lapusta 2021*. Zenodo. Retrieved from
 1015 <https://doi.org/10.5281/zenodo.5005276> doi: 10.5281/zenodo.5005276
- 1016 Heimisson, E. R., Dunham, E. M., & Almquist, M. (2019). Poroelastic effects
 1017 destabilize mildly rate-strengthening friction to generate stable slow slip
 1018 pulses. *Journal of the Mechanics and Physics of Solids*, 130, 262 – 279. doi:
 1019 10.1016/j.jmps.2019.06.007
- 1020 Heimisson, E. R., & Segall, P. (2018). Constitutive law for earthquake production
 1021 based on rate-and-state friction: Dieterich 1994 revisited. *Journal of Geophysi-*
 1022 *cal Research: Solid Earth*, 123(5), 4141–4156. doi: 10.1029/2018JB015656
- 1023 Hulikal, S., Lapusta, N., & Bhattacharya, K. (2018). Static and sliding contact of
 1024 rough surfaces: Effect of asperity-scale properties and long-range elastic in-
 1025 teractions. *Journal of the Mechanics and Physics of Solids*, 116, 217 - 238.
 1026 Retrieved from [http://www.sciencedirect.com/science/article/pii/](http://www.sciencedirect.com/science/article/pii/S0022509618300619)
 1027 [S0022509618300619](http://www.sciencedirect.com/science/article/pii/S0022509618300619) doi: <https://doi.org/10.1016/j.jmps.2018.03.022>
- 1028 Jha, B., & Juanes, R. (2014). Coupled multiphase flow and poromechanics:
 1029 A computational model of pore pressure effects on fault slip and earth-
 1030 quake triggering. *Water Resources Research*, 50(5), 3776-3808. doi:
 1031 10.1002/2013WR015175
- 1032 Jónsson, S., Segall, P., Pedersen, R., & Björnsson, G. (2003). Post-earthquake
 1033 ground movements correlated to pore-pressure transients. *Nature*, 424(6945),
 1034 179–183. doi: 10.1038/nature01776
- 1035 Linker, M. F., & Dieterich, J. H. (1992). Effects of variable normal stress on rock
 1036 friction: Observations and constitutive equations. *J. Geophys. Res. Solid*
 1037 *Earth*, 97(B4), 4923–4940. doi: 10.1029/92JB00017

- 1038 Liu, Y. (2013). Numerical simulations on megathrust rupture stabilized under strong
 1039 dilatancy strengthening in slow slip region. *Geophysical Research Letters*,
 1040 *40*(7), 1311-1316. doi: 10.1002/grl.50298
- 1041 Lockner, D. A., & Byerlee, J. D. (1994). Dilatancy in hydraulically isolated faults
 1042 and the suppression of instability. *Geophysical Research Letters*, *21*(22), 2353-
 1043 2356. doi: 10.1029/94GL02366
- 1044 Lyakhovskiy, V., & Ben-Zion, Y. (2020, 04). Isotropic seismic radiation from rock
 1045 damage and dilatancy. *Geophysical Journal International*, *222*(1), 449-460.
 1046 doi: 10.1093/gji/ggaa176
- 1047 Marone, C. (1998). Laboratory-derived friction laws and their application to seismic
 1048 faulting. *Annu. Rev. Earth Pl. Sc.*, *26*(1), 643-696.
- 1049 Marone, C., Raleigh, C. B., & Scholz, C. H. (1990). Frictional behavior and con-
 1050 stitutive modeling of simulated fault gouge. *Journal of Geophysical Research:*
 1051 *Solid Earth*, *95*(B5), 7007-7025. doi: 10.1029/JB095iB05p07007
- 1052 McNamee, J., & Gibson, R. E. (1960). Plane strain and axially symmetric problems
 1053 of the consolidation of a semi-infinite clay stratum. *Q. J. Mech. Appl. Math.*,
 1054 *13*(2), 210-227.
- 1055 Mitchell, T., & Faulkner, D. (2012). Towards quantifying the matrix permeability of
 1056 fault damage zones in low porosity rocks. *Earth Planet. Sc. Lett.*, *339*, 24-31.
- 1057 Platt, J. D., Rudnicki, J. W., & Rice, J. R. (2014). Stability and localization of
 1058 rapid shear in fluid-saturated fault gouge: 2. localized zone width and strength
 1059 evolution. *Journal of Geophysical Research: Solid Earth*, *119*(5), 4334-4359.
 1060 doi: 10.1002/2013JB010711
- 1061 Proctor, B., Lockner, D. A., Kilgore, B. D., Mitchell, T. M., & Beeler, N. M. (2020).
 1062 Direct evidence for fluid pressure, dilatancy, and compaction affecting slip in
 1063 isolated faults. *Geophysical Research Letters*, *47*(16), e2019GL086767. doi:
 1064 10.1029/2019GL086767
- 1065 Raimbourg, H., Famin, V., Palazzin, G., Yamaguchi, A., Augier, R., Kitamura,
 1066 Y., & Sakaguchi, A. (2019). Distributed deformation along the subduction
 1067 plate interface: The role of tectonic mélanges. *Lithos*, *334-335*, 69 - 87. doi:
 1068 <https://doi.org/10.1016/j.lithos.2019.01.033>
- 1069 Rice, J. R. (2006). Heating and weakening of faults during earthquake slip. *Journal*
 1070 *of Geophysical Research: Solid Earth*, *111*(B5). doi: 10.1029/2005JB004006

- 1071 Rice, J. R., & Cleary, M. P. (1976). Some basic stress diffusion solutions for fluid-
 1072 saturated elastic porous media with compressible constituents. *Rev. Geophys.*,
 1073 *14*(2), 227–241. doi: 10.1029/RG014i002p00227
- 1074 Rice, J. R., Lapusta, N., & Ranjith, K. (2001). Rate and state dependent friction
 1075 and the stability of sliding between elastically deformable solids. *J. Mech.*
 1076 *Phys. Solids*, *49*(9), 1865–1898.
- 1077 Rice, J. R., Rudnicki, J. W., & Platt, J. D. (2014). Stability and localization
 1078 of rapid shear in fluid-saturated fault gouge: 1. linearized stability analy-
 1079 sis. *Journal of Geophysical Research: Solid Earth*, *119*(5), 4311–4333. doi:
 1080 10.1002/2013JB010710
- 1081 Rice, J. R., & Ruina, A. (1983). Stability of steady frictional slipping. *J. Appl.*
 1082 *Mech.*, *50*(2), 343–349.
- 1083 Rice, J. R., & Simons, D. A. (1976). The stabilization of spreading shear faults
 1084 by coupled deformation-diffusion effects in fluid-infiltrated porous materials. *J.*
 1085 *Geophys. Res.*, *81*(29), 5322–5334. doi: 10.1029/JB081i029p05322
- 1086 Rubinstein, J. L., Vidale, J. E., Gomberg, J., Bodin, P., Creager, K. C., & Malone,
 1087 S. D. (2007). Non-volcanic tremor driven by large transient shear stresses.
 1088 *Nature*, *448*(7153), 579.
- 1089 Rudnicki, J. W., & Chen, C.-H. (1988). Stabilization of rapid frictional slip on a
 1090 weakening fault by dilatant hardening. *Journal of Geophysical Research: Solid*
 1091 *Earth*, *93*(B5), 4745–4757. doi: 10.1029/JB093iB05p04745
- 1092 Rudnicki, J. W., & Koutsibelas, D. A. (1991). Steady propagation of plane strain
 1093 shear cracks on an impermeable plane in an elastic diffusive solid. *Int. J.*
 1094 *Solids Struct.*, *27*(2), 205–225.
- 1095 Rudnicki, J. W., & Rice, J. R. (2006). Effective normal stress alteration due to
 1096 pore pressure changes induced by dynamic slip propagation on a plane be-
 1097 tween dissimilar materials. *J. Geophys. Res. Solid Earth*, *111*(B10). doi:
 1098 10.1029/2006JB004396
- 1099 Ruina, A. (1983). Slip instability and state variable friction laws. *Jour-*
 1100 *nal of Geophysical Research: Solid Earth*, *88*(B12), 10359–10370. doi:
 1101 10.1029/JB088iB12p10359
- 1102 Segall, P., & Lu, S. (2015). Injection-induced seismicity: Poroelastic and earthquake
 1103 nucleation effects. *J. Geophys. Res. Solid Earth*, *120*(7), 5082–5103.

- 1104 Segall, P., & Rice, J. R. (1995). Dilatancy, compaction, and slip instability of a
 1105 fluid-infiltrated fault. *Journal of Geophysical Research: Solid Earth*, *100*(B11),
 1106 22155–22171. doi: 10.1029/95JB02403
- 1107 Segall, P., & Rice, J. R. (2006). Does shear heating of pore fluid contribute to earth-
 1108 quake nucleation? *Journal of Geophysical Research: Solid Earth*, *111*(B9). doi:
 1109 <https://doi.org/10.1029/2005JB004129>
- 1110 Segall, P., Rubin, A. M., Bradley, A. M., & Rice, J. R. (2010). Dilatant strength-
 1111 ening as a mechanism for slow slip events. *J. Geophys. Res. Solid Earth*,
 1112 *115*(B12).
- 1113 Song, Y., & Rudnicki, J. W. (2017). Plane-strain shear dislocation on a leaky plane
 1114 in a poroelastic solid. *J. Appl. Mech.*, *84*(2), 021008.
- 1115 Templeton, E. L., & Rice, J. R. (2008). Off-fault plasticity and earthquake rup-
 1116 ture dynamics: 1. dry materials or neglect of fluid pressure changes. *Journal*
 1117 *of Geophysical Research: Solid Earth*, *113*(B9). doi: [https://doi.org/10.1029/](https://doi.org/10.1029/2007JB005529)
 1118 [2007JB005529](https://doi.org/10.1029/2007JB005529)
- 1119 Thomas, A. M., Nadeau, R. M., & Bürgmann, R. (2009). Tremor-tide correlations
 1120 and near-lithostatic pore pressure on the deep san andreas fault. *Nature*,
 1121 *462*(7276), 1048–1051. doi: 10.1038/nature08654
- 1122 Torabi, A., Braathen, A., Cuisiat, F., & Fossen, H. (2007). Shear zones in porous
 1123 sand: Insights from ring-shear experiments and naturally deformed sandstones.
 1124 *Tectonophysics*, *437*(1), 37 - 50. doi: 10.1016/j.tecto.2007.02.018
- 1125 Torberntsson, K., Stiernström, V., Mattsson, K., & Dunham, E. M. (2018, Jul 19).
 1126 A finite difference method for earthquake sequences in poroelastic solids. *Com-*
 1127 *putat. Geosci.*, *22*(5), 1351–1370. doi: 10.1007/s10596-018-9757-1
- 1128 Verruijt, A. (1971). Displacement functions in the theory of consolidation or in ther-
 1129 moelasticity. *Zeitschrift für angewandte Mathematik und Physik ZAMP*, *22*(5),
 1130 891–898.
- 1131 Viesca, R. C., & Dublanche, P. (2019). The slow slip of viscous faults. *Journal of*
 1132 *Geophysical Research: Solid Earth*, *124*(5), 4959–4983. doi: [https://doi.org/10](https://doi.org/10.1029/2018JB016294)
 1133 [.1029/2018JB016294](https://doi.org/10.1029/2018JB016294)
- 1134 Viesca, R. C., Templeton, E. L., & Rice, J. R. (2008). Off-fault plasticity and earth-
 1135 quake rupture dynamics: 2. effects of fluid saturation. *Journal of Geophysical*
 1136 *Research: Solid Earth*, *113*(B9). doi: <https://doi.org/10.1029/2007JB005530>

1137 Wibberley, C. A., & Shimamoto, T. (2003). Internal structure and permeability
1138 of major strike-slip fault zones: the Median Tectonic Line in Mie Prefecture,
1139 Southwest Japan. *J. Struct. Geol.*, 25(1), 59–78.